Ocean Engineering 275 (2023) 114154

Contents lists available at ScienceDirect

Ocean Engineering

journal homepage: www.elsevier.com/locate/oceaneng

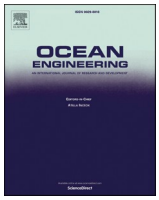

Mathematical modelling of nonlinear pressure drops in arbitrarily shaped port utilizing dual boundary element method

Prachi Priya [a], Prashant Kumar [a,*], Rajni [b]

[a] Department of Applied Sciences, National Institute of Technology Delhi, Delhi, 110040, India
[b] Jindal Global Business School, O. P. Jindal Global University, Sonipat, Haryana, 131001, India

ARTICLE INFO

Handling Editor: Prof. A.I. Incecik

Keywords:
Dual boundary element method
Wave trapping
Helmholtz equation
Porous barrier
Visakhapatnam port

ABSTRACT

A mathematical model is developed to analyze the wave-trapping characteristics of different types of porous and non-porous barriers in arbitrarily shaped domains utilizing the iterative Dual Boundary Element Method (DBEM) under the resonance conditions. In this analysis, Vertical, Wavy, Inverted V-shaped, and Inverted L-shaped barriers are utilized to investigate the effect of incident waves over the boundary of the harbor. The harbor is divided into an interconnected domain with variable bathymetry, and the Helmholtz equation is solved in each subdomain utilizing the prescribed boundary conditions. Further, the semi-empirical discharge equation with quadratic pressure drop is considered on the porous barrier to incorporate the effect of incident wave amplitude on the energy loss. The present numerical scheme is validated with existing studies and verified with convergence analysis. Further, the mathematical model is implemented on the Visakhapatnam port at four key locations with improved performance of different types of barriers. Moreover, the influence of the partial reflection coefficient is also investigated by considering the various combination of partially reflecting boundaries of the port. The wave trapping or absorbing characteristics of porous barriers proves an efficient tool to reduce the wave resonance inside the port.

1. Introduction

In coastal engineering, one of the major issues is the unpredictable behavior of the oceanic wave, and it disastrously affects the marine infrastructure such as ports, moored ships, mooring ropes, and fenders and also affects the waterfront populace. The coastal engineers consistently work to develop the technique to protect the coastal structures from destructive incident waves. One such approach is to build the barrier along with the coastal structures in the coastal regions. The barrier proves to be an efficient tool in reducing wave energy dissipation and creating a calmer area. Various researchers recommended that the barriers be installed such that they undergo an easy installation process, cost-effective, and are also effective for strong waves. The barriers are of various shapes, creating different influences on the resonance phenomenon, and also, the location of the barrier plays a vital role in reducing wave oscillation inside the port. Therefore, it is required to investigate the effectiveness of the barrier of different shapes with proper porosity placed in a suitable location in the coastal region. Coastal structures such as harbors, shelter ports, moored ships, mooring ropes, and fenders can be protected from the destructive incident wave that causes strong wave oscillations inside the coastal region.

Several numerical models developed to investigate the harbor resonance such as the Boundary element method (BEM) for the Helmholtz equation considering the constant depth and partial reflection along with multidirectional incident wave (Lee and Williams, 2002; Kumar et al., 2013, 2017), variable depth (Gaillard, 1982; Kumar et al., 2021) and Laplace equation including variable depth and partial reflection (Kumar and Gulshan, 2017, 2018; Chou and Han, 1993, 1994; Kumar et al., 2022), Finite-Element Method (FEM) (Ham and Bathe, 2012; Mercadé Ruiz et al., 2017) and Hybrid Finite-Element Method (HFEM) (Chang and Wang, 2017; Kumar and Rupali, 2018) based on mild slope equation to study the influence of diffraction, refraction, and partial reflection on the harbor's boundary for variable depth. The transient oceanic waves (Gao et al., 2019a, 2020) are mainly responsible for the extreme wave-induced oscillations inside the port, including the tsunami waves, such as solitary waves, double solitary waves, and N-waves (Dong et al., 2010; Gao et al., 2017, 2019b, 2021b). Serveral external forces such as focused wave groups (Kirby et al., 2003), infragravity waves (Gao et al., 2016), and seismic waves (Zheng et al., 2021), can cause wave-induced oscillations inside the port. Researchers (Dong

* Corresponding author.
E-mail address: prashantkumar@nitdelhi.ac.in (P. Kumar).

https://doi.org/10.1016/j.oceaneng.2023.114154
Received 10 April 2022; Received in revised form 8 February 2023; Accepted 7 March 2023
Available online 13 March 2023
0029-8018/© 2023 Elsevier Ltd. All rights reserved.

et al., 2013, 2020b, a; Gao et al., 2019b; González-Marco et al., 2008) employed numerical research to study the harbor oscillations induced by low-frequency wave groups and the physical experiments to investigate the transient harbor resonance (Dong et al., 2020a; Ma et al., 2021).

The researchers have made several enhancements to reduce the impact of destructive high-amplitude incident waves on the coastal structure. The construction of barriers in the coastal regions has gained enhanced attention in this field as it reduces the resonant frequency peak that emerges inside the port due to the accumulation of wave energy in the enclosed domains, which is a key aspect of the resonance problem. The objective of the porous barrier is to achieve maximal wave damping and, by altering the phase angle, restrict the incoming waves. The solid porous barriers are rubble-mound barriers or concrete caisson-type breakwaters (Sulisz, 2005, 2015; Koley et al., 2020). Traditionally, the complete protection breakwater, such as the rubble mound breakwater, is widely used to obstruct the water circulation near the coastal region (Panchang et al., 2008; Rageh and Koraim, 2010), but it requires massive capital expenses and mountain rocks. It drifts the researchers on the lookout for alternative breakwaters that are both cost-effective and provide better hydrodynamic performance. Thin porous barriers offer easy installation and are portable, cost-effective, and environmentally good. Thereafter, in Porto Torres industrial harbor, Italy, and Dalian Chemical Production Terminal, China, a system of thin porous walls with three and five confined chambers are developed to provide complete protection of ports from the destructive incident waves. An extensive study for thin structures (Ijima et al., 1975; Mattioli, 1981; Liu et al., 1986) are available such as vertical (Koley et al., 2015; Kaligatla et al., 2015; Bakhti et al., 2017), horizontal (Liu et al., 2008; An and Faltisen, 2012; Cho and Kim, 2013) to analyze the wave trapping characteristic of the barriers.

However, the wave interaction with a thin porous barrier is a complex phenomenon, and Darcy's law does not include the energy losses due to the variations in wave height and is not relevant to the high Reynolds number (Bennett et al., 1992). In an oscillatory flow, the pressure drops across the porous barrier, and the flow acceleration through the pores is a sum of quadratic drag components and an inertia term leads to the nonlinear pressure drop across the porous barrier was established by Molin in 2011. Liu and Li (2017) and Zhao et al. (2018) proposed a full solution based on an iterative analytical approach and boundary element method to analyze the wave interaction with porous breakwaters having nonlinear pressure drop. Recently (Zhao et al., 2020a,b; He et al., 2021), analyzed the gravity wave interaction with porous breakwater having a quadratic pressure drop using analytical approximations and numerically using DBEM (Nishad et al., 2021a; Venkateswarlu et al., 2021; Vijay et al., 2021). Hong and Chen developed the DBEM in 1988 to deal with the rank deficiency problem. It proves an efficient tool for solving the problem containing degenerate boundaries in a single domain (Chen et al., 2017; Zhao et al., 2020a,b; Nishad et al., 2021b). However, to analyze the proper model for the layout of the port, the study of resonance phenomena including breakwater considering the linear pressure drop were studied (Yu and Chwang, 1994) on the semi-circular harbor (Yip et al., 2001) in the circular harbor analytically. Chang and Wang (2017) utilized the Hybrid finite element method to investigate the wave response on the port in the presence of a permeable breakwater (Rupali and Kumar, 2021).

The study of wave-trapping characteristics of differently shaped porous barriers having nonlinear pressure drop boundary conditions over the realistic port is limited. Therefore, numerical model based on DBEM is developed to examine the wave energy dissipation effects, including the different configurations of porous breakwaters at various locations with partial reflection on the Visakhapatnam port, India. The wave amplification is examined at the resonant frequencies for the incident wave utilizing different types of barriers. In this paper, the fluid domain is divided into two main regions, Region-I, the open sea region, and Region-II, the interconnected port regions containing the multiple porous barriers placed in a suitable location inside the domain. The Helmholtz equation is solved in each region using dual integral equations, the singular integral equation at the port boundary and pseudo boundary (non-degenerate boundary) and one side of the porous barrier boundary (degenerate boundary) whereas hypersingular integral equation at the opposite side of the porous barrier boundary (degenerate boundary). The numerical scheme is validated by the available study of Lee (1971) and Shao et al. (2017) for the rectangular harbor in the absence of a breakwater and Yu and Chwang, 1994 for the semi-circular including porous breakwater. Moreover, the influence of variable wave absorbing/partial reflection boundaries and different configurations of porous breakwaters at different locations inside the Visakhapatnam port, Andhra Pradesh, India, is investigated. Based on the simulation results, some tactics, such as adding porous breakwaters and wave absorbers at the entrance and the port boundary, are suggested to reduce the resonance inside the Visakhapatnam port. The current numerical model provides an efficient tool to understand the wave amplification on any other realistic port/harbor connected to the open sea for practical applications.

2. Mathematical formulation

2.1. Model geometry

The mathematical model of propagation of waves in arbitrary port in the presence of wavy porous barriers is represented in Fig. 1, a Cartesian co-coordinate system (x, y, z) is used where the x-axis is directed along with the wave propagation, and the open-ocean is directed along the y-axis direction, and the variable ocean depth is along the z-axis. The fluid domain is divided into two regions, i.e., Region-I (open ocean region) (Ω_1) and Region-II (multiconnected port region) (Ω_2). The multiconnected port region is connected with common boundary (Γ_c) and is surrounded by the partially reflecting/absorbing boundary (Γ_h) of the port and connected with the open ocean region through a pseudo boundary (Γ_{ps}). The porous breakwaters are placed inside the port domain, termed as a degenerate boundary, as it can be placed at an arbitrary position in the port domain where Γ_{D_+} and Γ_{D_-} denotes the two sides of the degenerate boundary. The barriers are utilized to mitigate the wave-induced forces and incident wave energy dissipations inside the port region.

The fluid domain is assumed to be inviscid and incompressible, and the flow in the domain is considered to be irrotational; thus, from the potential flow theory, the velocity potential function will satisfy the Laplace equation, i.e.,

$$\nabla^2\varphi = 0 \tag{1}$$

The velocity potential function depends on the horizontal space vector (x, y), vertical space vector (z), and simple harmonic in time t, defined as

$$\varphi(x, y, z) = -\frac{igA_m}{\omega}\varphi(x, y)h(z)e^{-i\omega t} \tag{2}$$

where the depth function $h(z) = \frac{\cosh(k(h+z))}{\cosh(kh)}$, A_m represents the amplitude of the incident wave, i is the imaginary number $\sqrt{-1}$, g denotes the acceleration due to gravity, ω represents the angular frequency, and k represents the wave number satisfying the dispersion relation, i.e., $\omega^2 = kg\tanh(kh)$.

On substituting Eq. (2) in Eq. (1), the wave function (φ) satisfying the Helmholtz equation

$$\left(\nabla^2 + k^2\right)\varphi = 0 \tag{3}$$

(i) The boundary conditions defined on the free surface

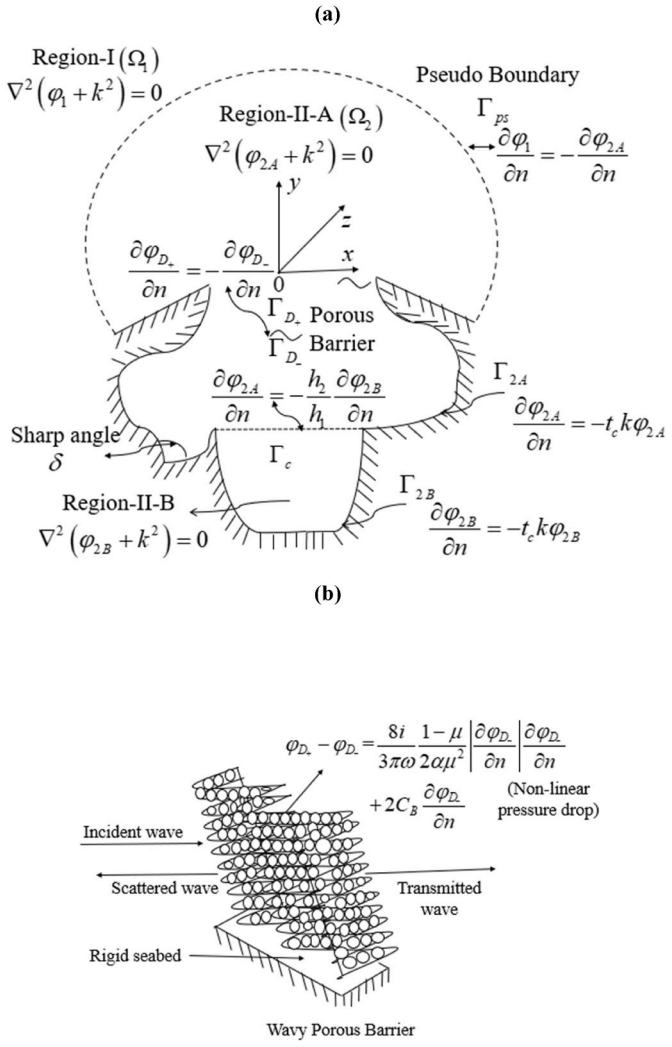

Fig. 1. (a) The geometry of the model defining the open ocean region (Region-I) and port region (Region-II) connected with pseudo boundary (Γ_{ps}) and surrounded with the partially reflecting multiconnected port ($\Gamma_h = \Gamma_{2A} \cup \Gamma_{2B}$) with common boundary ($\Gamma_C$) including the wavy barriers ($\Gamma_{D_+} \cup \Gamma_{D_-}$). **(b)** The analysis of waves through a wavy porous barrier.

$$\frac{\partial \varphi_j}{\partial n} - \frac{\omega^2 \varphi_j}{g} = 0, j = 1, 2 \tag{4}$$

(ii) The fluid does not penetrate on the sea bed and the boundary condition defined at sea bed as

$$\frac{\partial \varphi_j}{\partial n} = 0, j = 1, 2 \tag{5}$$

the subscript $j = 1$ denotes the open ocean region (Region-I), and $j = 2$ represents the port region which includes the Region-II-A and Region-II-B.

2.2. Solution of helmholtz equation (Region-I)

The solution of the wave potential function in Region-I comprises an incident, reflected, and scattered wave is given as

$$\varphi_1(x, y) = \varphi_i(x, y) + \varphi_r(x, y) + \varphi_{sct}(x, y) \tag{6}$$

Somerfield radiation boundary condition

$$\lim_{r\to\infty} \varphi_{sct} = 0, r = \sqrt{x^2 + y^2} \tag{7}$$

where φ_{sct} is the scattering wave function.

The solution of the scattered wave function φ_{sct} for Region-I follows Green's identity theorem

$$\varphi_{sct}\left(\vec{x}_f\right) = -\frac{i}{2}\int_\Gamma \left[\varphi_{sct}\frac{\partial}{\partial n}\left(H_0^1(kr)\right) - H_0^1(kr)\frac{\partial}{\partial n}(\varphi_{sct})\right] d\Gamma\left(\vec{x}_s\right) \tag{8}$$

where $\vec{x}_f \equiv (x_f, y_f)$ and $\vec{x}_s \equiv (x_s, y_s)$ and $H_0^1(kr)$ is the zeroth order Hankel function of the first kind. It represents the Green's function with first and second order derivatives are continuous within the domain and on the boundary of the domain. Where r is the distance between the source point $(\vec{x}_s)$ and field point $(\vec{x}_f)$. The Green's function $(H_0^1(kr) = J_0(kr) + iY_0(kr))$ and its normal derivative possesses the singularity as kr approaches to zero and hence require special treatment (Annexure-I).

2.3. Solution of helmholtz equation (Region-II)

The solution of the wave function in the port region requires the discretization of the boundary of the multiconnected port region that contains the port boundary ($\Gamma_h = \Gamma_{2A} \cup \Gamma_{2B}$) connected with the common boundary (Γ_C), pseudo boundary (Γ_{ps}), and the degenerate porous barriers boundary ($\Gamma_{D_+} \cup \Gamma_{D_-}$). The free surface and sea bed boundary condition is defined in Eq. (4) and Eq. (5), and the remaining prescribed boundary conditions are defined as

(a) Partiaslly reflecting/absorbing boundary on the port wall ($\Gamma_h = \Gamma_{2A} \cup \Gamma_{2B}$).

The boundary of the port with either fully reflecting or fully absorbing is inappropriate for applying real topographies. As some part absorbs at the port boundary and some parts are reflected in the ocean, the partially reflecting boundary condition (Isaacson and Qu, 1990) is suitable for analyzing the wave oscillation on the actual topography as

$$\frac{\partial \varphi_2}{\partial n} = -t_c k \varphi_2 \quad \text{on } \Gamma_h, \tag{9}$$

where t_c is the complex transmission coefficient defined in the interval [0, 1], and it is given in terms of reflection coefficient R_{coeff}:

$$\mathrm{Re}(t_c) = 0 \text{ and } \mathrm{Im}(t_c) = \frac{1 - R_{coeff}}{1 + R_{coeff}}, \tag{10}$$

when $R_{coeff} = 1$ for the fully reflective boundary conditions result in no flux condition on the boundary, and $R_{coeff} = 0$ for the full wave absorption on the boundary of the port.

(b) Continuity boundary condition at the common boundary (Γ_c)s

The bathymetry of the port domain cannot be unanimous. To include the variable bathymetry, the port domain is divided into sub-regions, Region-II-A and Region-II-B, considering the average water depth in each sub-region, assuming that the water depth near the open sea region is greater than the depth away from the open sea region $h_1 \geq h_2$ (see Fig. 2). The continuity condition at the boundary PQ for the mass and the energy fluxes whereas no flux boundary condition is satisfied at the solid wall QR is given as

$$\begin{aligned} &\frac{\partial \varphi_{2A}}{\partial n} = -\frac{\partial \varphi_{2B}}{\partial n}, \varphi_{2A} = \varphi_{2B} \quad 0 \leq z \leq -h_2 \\ &\frac{\partial \varphi_{2A}}{\partial n} = 0 \quad h_2 \leq z \leq -h_1 \end{aligned} \tag{11}$$

Now multiplying the $\cosh k(h_1 + z)$ on the left-hand side and

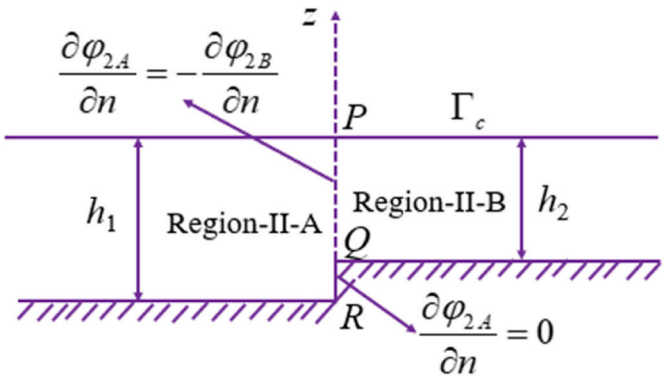

Fig. 2. Distribution of approximate variable bathymetry in the harbour's interconnected regions Region-II-A and Region-II-B with water depths h_1 and h_2.

$\cosh k(h_2+z)$ on the right-hand side of the normal derivative of the wave function and integrating to consider the depth in each region, the matching boundary condition at the common boundary is obtained as

$$\frac{\partial \varphi_{2A}}{\partial n} = -\frac{h_2}{h_1}\frac{\partial \varphi_{2B}}{\partial n}, \varphi_{2A} = \varphi_{2B} \tag{12}$$

(c) Boundary condition on the porous breakwater

The porous breakwaters are developed to minimize the impact of high amplitude incident waves inside the coastal region such that it is cost-effective, reliable, and easy to install. The porous breakwater is placed at an appropriate location inside the port region to reduce the wave forces inside the port. The porous breakwater is treated as a degenerate boundary, and the continuity condition is imposed on the both sides of the breakwater is given as follows

$$\frac{\partial \varphi_{D_+}}{\partial n} = -\frac{\partial \varphi_{D_-}}{\partial n}, \tag{13}$$

where φ_{D_+} and φ_{D_-} denotes the potential function at the two sides of the degenerate breakwater Γ_{D_+} and Γ_{D_-} respectively (see Fig. 1a). The fluid velocity is assumed to be continuous at the porous breakwaters, and the negative sign in Eq. (13) is due to the outward normal vector in the opposite direction. ($\vec{n}$).

The semi-empirical discharge equation having quadratic pressure drop follows the flow past over the porous structure and is derived by Molin and Remy (2015). The pressure drops over the porous breakwater are proportional to the sum of the square of the normal velocity of the fluid (quadratic drag term), and the inertia term, which is given as

$$\varphi_{D_-} - \varphi_{D_+} = \frac{8i}{3\pi\omega}\frac{1-\mu}{2\alpha\mu^2}\left|\frac{\partial \varphi_{D_-}}{\partial n}\right|\frac{\partial \varphi_{D_-}}{\partial n} + 2C_B\frac{\partial \varphi_{D_-}}{\partial n}, \tag{14}$$

where μ, C_B and α represents the porosity of the barriers, inertial coefficient, and discharge coefficient, respectively. The first two terms of the right-hand side of Eq. (14) represent the energy dissipation effect, and the inertial effect of the perforated wall, respectively. According to Suh et al. (2011) and Huang et al. (2011), the inertia coefficient is defined as $C_B = \delta/2\ \mu$ and δ is the thickness of the wall.

(d) Matching boundary conditions at the pseudo boundary (Γ_{ps}) is given as

$$\varphi_1 = \varphi_{2A}, \frac{\partial \varphi_1}{\partial n} = -\frac{\partial \varphi_{2A}}{\partial n}, \tag{15}$$

The port region is surrounded by pseudo boundary, partially reflecting boundaries including the degenerate breakwaters. Thus, the solution follows Green's identity theorem as

$$\varphi_2\left(\vec{x}_f\right) = a\int_\Gamma\left[\varphi_2\frac{\partial H_0^1(kr)}{\partial n} - H_0^1(kr)\frac{\partial \varphi_2}{\partial n}\right]d\Gamma\left(\vec{x}_s\right), \Gamma = \Gamma_{ps}\cup\Gamma_h\cup\Gamma_{D_+} \cup\Gamma_{D_-}, \tag{16}$$

where $\vec{x}_f \equiv (x_f, y_f)$ and $\vec{x}_s \equiv (x_s, y_s)$, the parameter a is defined as

$$a = \begin{cases} -i/4 & \text{at any interior points,} \\ -i/2 & \text{at bondary points,} \\ 0 & \text{at any outer points} \end{cases} \tag{17}$$

and $H_0^1(kr)$ is the Hankel function of first kind zero-order, where$r$ is defined as

$$r = \sqrt{\left(x_f - x_s\right)^2 + \left(y_f - y_s\right)^2}. \tag{18}$$

The poroubreakwater has finite thickness not larger than a fraction of the wavelength of the incoming wave. Eq. (16) is not sufficient to obtain a unique solution in the case of a zero-thickness of the degenerate porous breakwater. Thus, the system of singular and hyper-singular boundary integral equations is obtained across the boundaries of thin (zero-thickness) porous breakwater by considering the boundary points on the two sides of the degenerate porous boundary. The singular boundary integral equation is given as

$$\varphi_2\left(\vec{x}_f\right) = a\int_\Gamma\left[\varphi_2\frac{\partial H_0^1(kr)}{\partial n_s} - H_0^1(kr)\frac{\partial \varphi_2}{\partial n_s}\right]d\Gamma\left(\vec{x}_s\right) \tag{19}$$

The hyper-singular boundary integral equation is given as

$$\frac{\partial \varphi_2\left(\vec{x}_f\right)}{\partial n_f} = a\int_\Gamma\left[\varphi_2\frac{\partial^2 H_0^1(kr)}{\partial n_f \partial n_s} - \frac{\partial H_0^1(kr)}{\partial n_f}\frac{\partial \varphi_2}{\partial n_s}\right]d\Gamma\left(\vec{x}_s\right) \tag{20}$$

The boundary of the port domain is divided into multiconnected domains, namely, Region-II-A and Region-II-B. The porous breakwater is treated as a degenerate boundary that can be placed in any region at any position. The porous breakwater is placed in Region-II-A, then the solution for the wave function in Region-II-A follows the singular and hyper-singular boundary integral equation. The problem including a non-degenerate ($\Gamma_{ND} = \Gamma_{ps}\cup\Gamma_{2A}\cup\Gamma_c$), and the degenerate boundary ($\Gamma_{D_+}\cup\Gamma_{D_-}$), Γ_{D_+} is opposite to that of Γ_{D_-}, Eqs. (19) and (20), is reformulated respectively when the field point ($\vec{x}_f$) belongs to the non-degenerate boundary ($\Gamma_{ND} = \Gamma_{ps}\cup\Gamma_{2A}\cup\Gamma_C$) as

$$\varphi_{2A}\left(\vec{x}_f\right) = -\frac{i}{2}\int_{\Gamma_{ND}}\left[\varphi_{2A}\left(\vec{x}_s\right)\frac{\partial H_0^1(kr)}{\partial n_s} - H_0^1(kr)\frac{\partial \varphi_{2A}\left(\vec{x}_s\right)}{\partial n_s}\right]d\Gamma\left(\vec{x}_s\right) - \frac{i}{2}\int_{\Gamma_{D_+}}\left[\varphi_{2A}\left(\vec{x}_{\Gamma_{DS}}\right)\frac{\partial H_0^1(kr)}{\partial n_s} - H_0^1(kr)\frac{\partial \varphi_{2A}\left(\vec{x}_{\Gamma_{DA}}\right)}{\partial n_s}\right]d\Gamma\left(\vec{x}_s\right) \tag{21}$$

$$\frac{\partial \varphi_{2A}\left(\vec{x}_f\right)}{\partial n_f} = -\frac{i}{2}\int_{\Gamma_{ND}}\left[\varphi_{2A}\left(\vec{x}_s\right)\frac{\partial^2 H_0^1(kr)}{\partial n_f \partial n_s} - \frac{\partial H_0^1(kr)}{\partial n_f}\frac{\partial \varphi_{2A}\left(\vec{x}_s\right)}{\partial n_s}\right]d\Gamma\left(\vec{x}_s\right) - \frac{i}{2}\int_{\Gamma_{D_+}}\left[\varphi_{2A}\left(\vec{x}_{\Gamma_{DS}}\right)\frac{\partial^2 H_0^1(kr)}{\partial n_f \partial n_s} - \frac{\partial H_0^1(kr)}{\partial n_f}\frac{\partial \varphi_{2A}\left(\vec{x}_{\Gamma_{DA}}\right)}{\partial n_s}\right]d\Gamma\left(\vec{x}_s\right) \tag{22}$$

where, $\varphi_{2A}(\vec{x}_{\Gamma_{DS}}) = \varphi_{2A}(\vec{x}_{\Gamma_{D_+}}) - \varphi_{2A}(\vec{x}_{\Gamma_{D_-}})$ and $\frac{\partial \varphi_{2A}(\vec{x}_{\Gamma_{DA}})}{\partial n_s} =$

$\frac{\partial\varphi_{2A}(\vec{x}_{\Gamma_{D_+}})}{\partial n_s}+\frac{\partial\varphi_{2A}(\vec{x}_{\Gamma_{D_-}})}{\partial n_s}$,

when the field point $(\vec{x}_f)$ belong to the degenerate boundary (Γ_{D_+}), Eq. (19) and Eq. (20) is formulated as

$$\varphi_{2A}\left(\vec{x}_{\Gamma_{DA}}\right)=-\frac{i}{2}\int_{\Gamma_{ND}}\left[\varphi_{2A}\left(\vec{x}_s\right)\frac{\partial H_0^1(kr)}{\partial n_s}-H_0^1(kr)\frac{\partial\varphi_{2A}\left(\vec{x}_s\right)}{\partial n_s}\right]d\Gamma\left(\vec{x}_s\right)-\frac{i}{2}\int_{\Gamma_{D_+}}\left[\varphi_{2A}\left(\vec{x}_{\Gamma_{DS}}\right)\frac{\partial H_0^1(kr)}{\partial n_s}-H_0^1(kr)\frac{\partial\varphi_{2A}\left(\vec{x}_{\Gamma_{DA}}\right)}{\partial n_s}\right]d\Gamma\left(\vec{x}_s\right) \tag{23}$$

$$\frac{\partial\varphi_{2A}\left(\vec{x}_{\Gamma_{DS}}\right)}{\partial n_f}=-\frac{i}{2}\int_{\Gamma_{ND}}\left[\varphi_{2A}\left(\vec{x}_s\right)\frac{\partial^2 H_0^1(kr)}{\partial n_f\partial n_s}-\frac{\partial H_0^1(kr)}{\partial n_f}\frac{\partial\varphi_{2A}\left(\vec{x}_s\right)}{\partial n_s}\right]d\Gamma\left(\vec{x}_s\right)-\frac{i}{2}\int_{\Gamma_{D_+}}\left[\varphi_{2A}\left(\vec{x}_{\Gamma_{DS}}\right)\frac{\partial^2 H_0^1(kr)}{\partial n_f\partial n_s}-\frac{\partial H_0^1(kr)}{\partial n_f}\frac{\partial\varphi_{2A}\left(\vec{x}_{\Gamma_{DA}}\right)}{\partial n_s}\right]d\Gamma\left(\vec{x}_s\right) \tag{24}$$

where, $\varphi_{2A}(\vec{x}_{\Gamma_{DA}})=\varphi_{2A}(\vec{x}_{\Gamma_{D_+}})+\varphi_{2A}(\vec{x}_{\Gamma_{D_-}})$ and $\frac{\partial\varphi_{2A}(\vec{x}_{\Gamma_{DS}})}{\partial n_s}=\frac{\partial\varphi_{2A}(\vec{x}_{\Gamma_{D_+}})}{\partial n_s}-\frac{\partial\varphi_{2A}(\vec{x}_{\Gamma_{D_-}})}{\partial n_s}$.

where Γ_{ps} represents the pseudo boundary, Γ_{2A} represents the harbor boundary of the Region-II-A, and Γ_c represents the common boundary of Region-II-A and Region-II-B, while the two sides of degenerate porous boundary are denoted with $\Gamma_{D_+}\cup\Gamma_{D_-}$.

The solution for the wave function in Region-II-B follows

$$\varphi_{2B}\left(\vec{x}_f\right)=a\int_{\Gamma}\left[\varphi_{2B}\frac{\partial H_0^1(kr)}{\partial n_s}-H_0^1(kr)\frac{\partial\varphi_{2B}}{\partial n_s}\right]d\Gamma\left(\vec{x}_s\right),\Gamma=\Gamma_{2B}\cup\Gamma_C \tag{25}$$

2.4. Spectral discretization

The spectral discretization is used to compute the ideal solution for collocation points, and the process involves the estimation of function by the Chebyshev polynomial ($T_n(c)=\cos(n\cos^{-1}c)$) as an interpolating polynomial over an interval [−1, 1]. The boundary of the domain is divided into a finite number of segments, and each segment is further subdivided into a semi-circle of the unit radius using Chebyshev discretization; the discretized points are the zeros of the Chebyshev polynomial lie in the range [−1, 1] and are defined by

$$c_j=\cos\left(\frac{j\pi}{N_i}\right),j=0,1,2,\ldots\ldots,N_i \tag{26}$$

where N_i denotes the total number of discretized points on the i^{th} boundary. The corresponding jth point of the i^{th} segment is given as

$$\vec{x}_j=\vec{x}_{N_{i-1}}+\frac{1}{2}(c_j+1)\left(\vec{x}_{N_i}-\vec{x}_{N_{i-1}}\right)$$
$$\vec{y}_j=\vec{y}_{N_{i-1}}+\frac{1}{2}(c_j+1)\left(\vec{y}_{N_i}-\vec{y}_{N_{i-1}}\right) \tag{27}$$

Finally, the wave function for each region may be computed by discretizing each segment using spectral discretization and changing the appropriate boundary integral using Jacobian transformation, thus, Eq. (8), Eq. (21), Eq. (22), Eq. (23), Eq. (24), and Eq. (25) are written as

$$\varphi_{sct}(\vec{x})=-\frac{i}{2}\sum_{l=1}^{N}\int_{-1}^{1}\left[\varphi_{sct}\left(\vec{x}_0\right)\frac{\partial}{\partial n}\left(H_0^1(kr)\right)-H_0^1(kr)\frac{\partial}{\partial n}\left(\varphi_{sct}\left(\vec{x}_0\right)\right)\right]J^l dc \tag{28}$$

$$\varphi_{2A}\left(\vec{x}_f\right)=-\frac{i}{2}\sum_{l=1}^{ND}\int_{-1}^{1}\left[\varphi_{2A}\left(\vec{x}_s\right)\frac{\partial H_0^1(kr)}{\partial n_s}-H_0^1(kr)\frac{\partial\varphi_{2A}\left(\vec{x}_s\right)}{\partial n_s}\right]J^l dc-\frac{i}{2}\sum_{l=1}^{D_+}\int_{-1}^{1}\left[\varphi_{2A}\left(\vec{x}_{\Gamma_{DS}}\right)\frac{\partial H_0^1(kr)}{\partial n_s}-H_0^1(kr)\frac{\partial\varphi_{2A}\left(\vec{x}_{\Gamma_{DA}}\right)}{\partial n_s}\right]J^l dc \tag{29}$$

$$\frac{\partial\varphi_{2A}\left(\vec{x}_f\right)}{\partial n_f}=-\frac{i}{2}\sum_{l=1}^{ND}\int_{-1}^{1}\left[\varphi_{2A}\left(\vec{x}_s\right)\frac{\partial^2 H_0^1(kr)}{\partial n_f\partial n_s}-\frac{\partial H_0^1(kr)}{\partial n_f}\frac{\partial\varphi_{2A}\left(\vec{x}_s\right)}{\partial n_s}\right]J^l dc-\frac{i}{2}\sum_{l=1}^{D_+}\int_{-1}^{1}\left[\varphi_{2A}\left(\vec{x}_{\Gamma_{DS}}\right)\frac{\partial^2 H_0^1(kr)}{\partial n_f\partial n_s}-\frac{\partial H_0^1(kr)}{\partial n_f}\frac{\partial\varphi_{2A}\left(\vec{x}_{\Gamma_{DA}}\right)}{\partial n_s}\right]J^l dc \tag{30}$$

$$\varphi_{2A}\left(\vec{x}_{\Gamma_{DA}}\right)=-\frac{i}{2}\sum_{l=1}^{ND}\int_{-1}^{1}\left[\varphi_{2A}\left(\vec{x}_s\right)\frac{\partial H_0^1(kr)}{\partial n_s}-H_0^1(kr)\frac{\partial\varphi_{2A}\left(\vec{x}_s\right)}{\partial n_s}\right]J^l dc-\frac{i}{2}\sum_{l=1}^{D_+}\int_{-1}^{1}\left[\varphi_{2A}\left(\vec{x}_{\Gamma_{DS}}\right)\frac{\partial H_0^1(kr)}{\partial n_s}-H_0^1(kr)\frac{\partial\varphi_{2A}\left(\vec{x}_{\Gamma_{DA}}\right)}{\partial n_s}\right]J^l dc \tag{31}$$

$$\frac{\partial\varphi_{2A}\left(\vec{x}_{\Gamma_{DS}}\right)}{\partial n_f}=-\frac{i}{2}\sum_{l=1}^{ND}\int_{-1}^{1}\left[\varphi_{2A}\left(\vec{x}_s\right)\frac{\partial^2 H_0^1(kr)}{\partial n_f\partial n_s}-\frac{\partial H_0^1(kr)}{\partial n_f}\frac{\partial\varphi_{2A}\left(\vec{x}_s\right)}{\partial n_s}\right]J^l dc-\frac{i}{2}\sum_{l=1}^{D_+}\int_{-1}^{1}\left[\varphi_{2A}\left(\vec{x}_{\Gamma_{DS}}\right)\frac{\partial^2 H_0^1(kr)}{\partial n_f\partial n_s}-\frac{\partial H_0^1(kr)}{\partial n_f}\frac{\partial\varphi_{2A}\left(\vec{x}_{\Gamma_{DA}}\right)}{\partial n_s}\right]J^l dc \tag{32}$$

$$\varphi_{2B}\left(\vec{x}_f\right)=-\frac{i}{2}\sum_{l=1}^{NB+NC}\int_{-1}^{1}\left[\varphi_{2B}\frac{\partial H_0^1(kr)}{\partial n_s}-H_0^1(kr)\frac{\partial\varphi_{2B}}{\partial n_s}\right]J^l dc \tag{33}$$

where, J^l represents the Jacobian transformation for the lth boundary segment of each region and is calculated as follows:

$$J^l=\frac{\sqrt{(x_l-x_{l-1})^2+(y_l-y_{l-1})^2}}{2}, \tag{34}$$

On combining Eq. (6) and Eq. (28) and utilizing the matching boundary condition at the pseudo boundary from Eq. (15) and the pseudo boundary is discretized using Spectral discretization, the matrix form is obtained as

$$[\varphi_{2A}]_{\Gamma_{ps}}=[M_1]\left[(\varphi_{2A})_n\right]_{\Gamma_{ps}}+[V_0]_{\Gamma_{ps}} \tag{35}$$

where,

$$[M_1]=-[H_s]^{-1}[H] \tag{36}$$

$$[V_0] = [\varphi_{IR}] + [M_1]\left[(\varphi_{IR})_n\right]_{\Gamma_{ps}} \tag{37}$$

where, $\varphi_{IR} = \varphi_i + \varphi_r$ and $[H] = \left(-\frac{i}{2}\int_{\Gamma} H_0^1(kr)d\Gamma\right)_{ij}$, $[H_s] = \left(-\frac{i}{2}\int_{\Gamma}\frac{\partial H_0^1(kr)}{\partial n_s}d\Gamma\right)_{ij} - \delta_{ij}$..

The boundary of Region-II-A is discretized into *NA* constant grid points utilizing Spectral discretization in a counter-clockwise sense. Eq. (29) to Eq. (32) is rewritten in a matrix form as follows,

$$[H]\left[(\varphi_{2A})_n\right] = [H_s][\varphi_{2A}] \tag{38}$$

$$\left[H_f\right]\left[(\varphi_{2A})_n\right] = \left[H_{sf}\right][\varphi_{2A}] \tag{39}$$

and the boundary of Region-II-B is discretized into *NB* constant grid points, and Eq. (33) is written in matrix

$$[H]\left[(\varphi_{2B})_n\right] = [H_s][\varphi_{2B}] \tag{40}$$

where, $[H_f] = \left(-\frac{i}{2}\int_{\Gamma}\frac{\partial H_0^1(kr)}{\partial n_f}d\Gamma\right)_{ij} + \delta_{ij}$ and $[H_{sf}] = \left(-\frac{i}{2}\int_{\Gamma}\frac{\partial^2 H_0^1(kr)}{\partial n_f \partial n_s}d\Gamma\right)_{ij}$.

On substituting the boundary condition of the partially reflecting boundary of the Region-II-B, Eq. (33) is expressed as

$$[\varphi_{2B}] = [M_2]\left[(\varphi_{2B})_n\right] \tag{41}$$

where, $[M_2] = [[H_s] - [H][U0]]^{-1}[H]$ and $[U0] = \begin{bmatrix} 0 & 0 & 0\,0 & \\ 0 & ikt_c\,[I_{2B}] & & 0\,0 \\ 0 & 0 & 0\,0 & \\ 0 & 0 & 0\,0 & \end{bmatrix}$.

On utilizing the matching boundary condition at the common boundary (Γ_c) of Region-II-A and Region-II-B and

$$[\varphi_{2A}] = [M_3]\left[(\varphi_{2A})_n\right] \tag{42}$$

where, $[M_3] = [M_{21}]_{ij}$; $i = NC, NC-1, \cdots\cdots 2, 1$ and $j = 1, 2, \cdots\cdots NC-1, NC$,

$$[M_{21}] = [M_2][U1] \text{ and } [U1] = \frac{h_2}{h_1}\begin{bmatrix} \begin{bmatrix} 0 \cdots\cdots -1 \\ \cdots\cdots\cdots \\ -1 \cdots\cdots 0 \end{bmatrix}_{NC\times NC} \\ 0 \end{bmatrix}.$$

Now, on combining Eq. (38) and Eq. (39) and employing the method of (Chen et al., 2002, 2004)

$$\begin{bmatrix} H_{\Gamma_R\Gamma_R} & H_{\Gamma_R\Gamma_{21}} & H_{\Gamma_R\Gamma_{22}} \\ H_{\Gamma_{21}\Gamma_R} & H_{\Gamma_{21}\Gamma_{21}} & H_{\Gamma_{21}\Gamma_{22}} \\ H_{f_{\Gamma_{21}\Gamma_R}} & H_{f_{\Gamma_{21}\Gamma_{21}}} & H_{f_{\Gamma_{21}\Gamma_{22}}} \end{bmatrix}\begin{bmatrix} \left[(\varphi_{2A})_n\right]_{\Gamma_R} \\ \left[(\varphi_{2A})_n\right]_{\Gamma_{D_+}} \\ \left[(\varphi_{2A})_n\right]_{\Gamma_{D_-}} \end{bmatrix} = \begin{bmatrix} H_{s\Gamma_R\Gamma_R} & H_{s\Gamma_R\Gamma_{21}} & H_{s\Gamma_R\Gamma_{22}} \\ H_{s\Gamma_{21}\Gamma_R} & H_{s\Gamma_{21}\Gamma_{21}} & H_{s\Gamma_{21}\Gamma_{22}} \\ H_{sf_{\Gamma_{21}\Gamma_R}} & H_{sf_{\Gamma_{21}\Gamma_{21}}} & H_{sf_{\Gamma_{21}\Gamma_{22}}} \end{bmatrix}\begin{bmatrix} (\varphi_{2A})_{\Gamma_R} \\ (\varphi_{2A})_{\Gamma_{D_+}} \\ (\varphi_{2A})_{\Gamma_{D_-}} \end{bmatrix} \tag{43}$$

Eq. (43) is rewritten as

$$\left[HH_f\right][\varphi_{2A_n}] = \left[H_sH_{sf}\right][\varphi_{2A}] \tag{44}$$

where Γ_R represents the non-degenerate boundary i.e. $\Gamma_R = \Gamma_{ps} \cup \Gamma_{2A} \cup \Gamma_C$.

The matrix obtained includes the integration of the Hankel function, and its first order and second-order derivative singularity arise for the diagonal terms requires special attention (Annexure-I). On substituting the prescribed boundary condition and the obtained boundary condition at pseudo boundary and common boundary from Eq. (35) and Eq. (42) in Eq. (44), we get

$$[Q][X] = [V] \tag{45}$$

where,

$$[X] = \left[(\varphi_n)_{\Gamma_{ps}}, \varphi_{\Gamma_{2A_1}}, (\varphi_n)_{\Gamma_C}, \varphi_{\Gamma_{2A_2}}, \varphi_{\Gamma_{D_+}}, (\varphi_n)_{\Gamma_{D_+}}\right]^T \text{ and } [V] = \left[H_sH_{sf}\right]\left[(V_0)_{\Gamma_{ps}}\,0\,0\,000\right]^T \tag{46}$$

and the matrix Q is

$$[Q] = \left[HH_f\right][U2] + \left[HH_f\right][U3] - \left[H_sH_{sf}\right][U4] - \left[H_sH_{sf}\right][U5] \tag{47}$$

where,

$$[U2] = \begin{bmatrix} [I_{ps}] & 0 & 0 & 0 & 0 & 0 \\ 0 & ikt_c\,[I_{2A_1}] & 0 & 0 & 0 & 0 \\ 0 & 0 & [I_{NC}] & 0 & 0 & 0 \\ 0 & 0 & 0 & ikt_c\,[I_{2A_2}] & 0 & 0 \\ 0 & 0 & 0 & 0 & 0 & 0 \\ 0 & 0 & 0 & 0 & 0 & 0 \end{bmatrix}, [U3] = \begin{bmatrix} 0\,0\,0 & 0\,0 & 0 \\ 0\,0\,0 & 0\,0 & 0 \\ 0\,0\,0 & 0\,0 & 0 \\ 0\,0\,0 & 0\,0 & 0 \\ 0\,0\,0 & 0\,0 & [I_B] \\ 0\,0\,0 & 0\,0 & -[I_B] \end{bmatrix},$$

$$[U4] = \begin{bmatrix} [M_1] & 0 & 0 & 0 & 0 & 0 \\ 0 & [I_{2A_1}] & 0 & 0 & 0 & 0 \\ 0 & 0 & [M_3] & 0 & 0 & 0 \\ 0 & 0 & 0 & [I_{2A_2}] & 0 & 0 \\ 0 & 0 & 0 & 0 & [I_B]\,0 & \\ 0 & 0 & 0 & 0 & [I_B]\,0 & \end{bmatrix}, [U5] = \begin{bmatrix} 000\,0 & 0 & 0 \\ 000\,0 & 0 & 0 \\ 000\,0 & 0 & 0 \\ 000\,0 & 0 & 0 \\ 000\,0 & 0 & 0 \\ 000\,0 & 0 & [diag(P)] \end{bmatrix}. \tag{48}$$

where, $P = \frac{8i}{3\pi\omega}\frac{1-\mu}{2\alpha\mu^2}\left|\frac{\partial\varphi_{21}}{\partial n}\right| + 2C_B$.

The boundary condition on the porous barriers is nonlinear (i.e., quadratic); obtaining a numerical solution is not straightforward. Therefore, an iterative procedure is adopted given in Liu and Li (2017). The potential function is calculated in/out of the port domain, and the present formulation can be modified for arbitrary number of interconnected domains. Thus, the wave amplification factor (A_f) is determined in the bounded region as

$$A_f = \frac{|\varphi_i(x,y)|}{|\varphi_{IR}|}, i = 1, 2 \tag{49}$$

The numerical solution is presented for two interconnected regions (Eq. (49)) and similarly, amplification can also be obtained for the three interconnected regions including the porous barriers. The porous barrier is placed in any region as a degenerate boundary and the dual interal, i.e., singular and hypersingular integral equations (Eq. (19) and Eq. (20)). is solved in that region. In remaining regions, the singular integral equation (Eq. (19)) is sufficient to obtain the wave function utilizing the prescribed boundary conditions. Once the wave function and its normal derivative are calculated at the boundary of all interconnected regions, the wave function is obtained inside the port at any location and thus wave amplification is calculated from Eq. (49). Eq. (49) is also applied on rectangular port and Visakhapatnam port.

3. Validation and convergence

3.1. Numerical validation

The numerical method is discussed above is implemented on a rectangular port of length 1.208 m, breadth 0.198 m, and the radius of the pseudo boundary is 0.2 m with the normal incident wave is interacting to the boundary of the port considering the porous barrier of different shapes (Fig. 3) and fully reflecting port ($R_{coeff} = 1$) to obtain the accuracy of the present scheme. There are four types of a porous barrier placed at the entrance (a) horizontal barrier, (b) wavy barrier, (c) inverted V-shaped barrier, and (d) inverted L-shaped porous barriers.

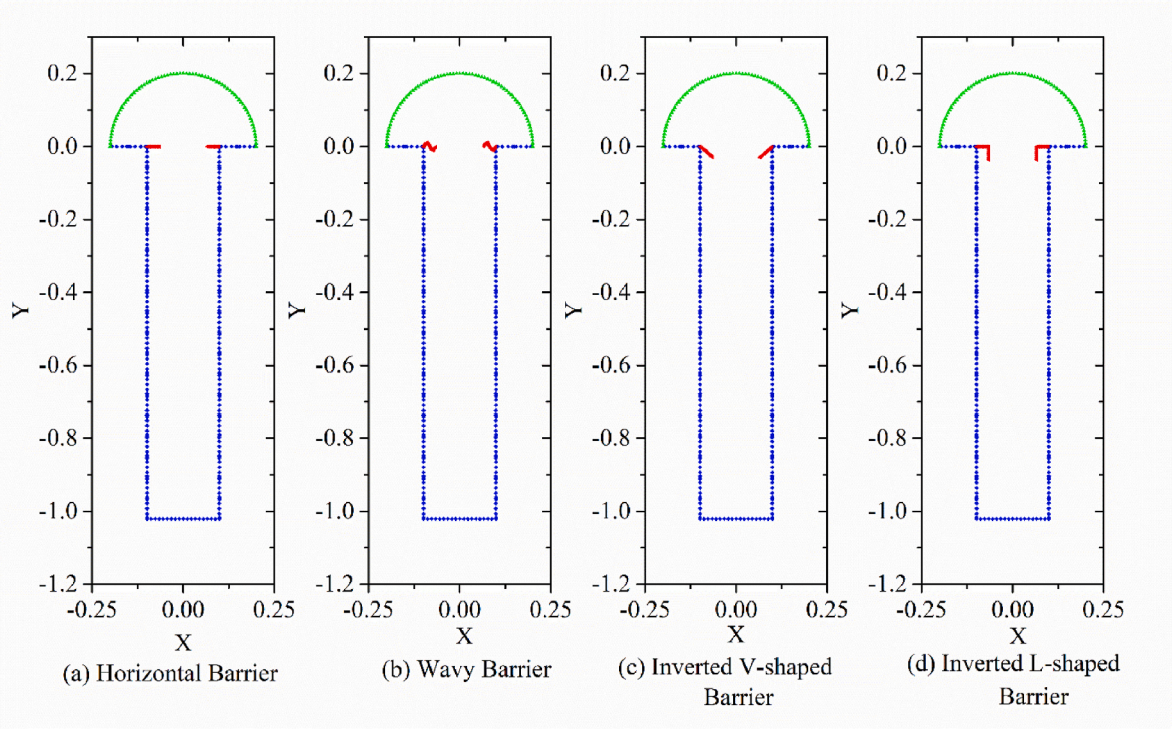

Fig. 3. The domain discretization of the rectangular harbor includes the degenerate barrier (a) Horizontal barrier, (b) Wavy barrier, (c) Inverted V-shaped barrier, and (d) Inverted L-shaped porous barriers at the two sides of the entrance.

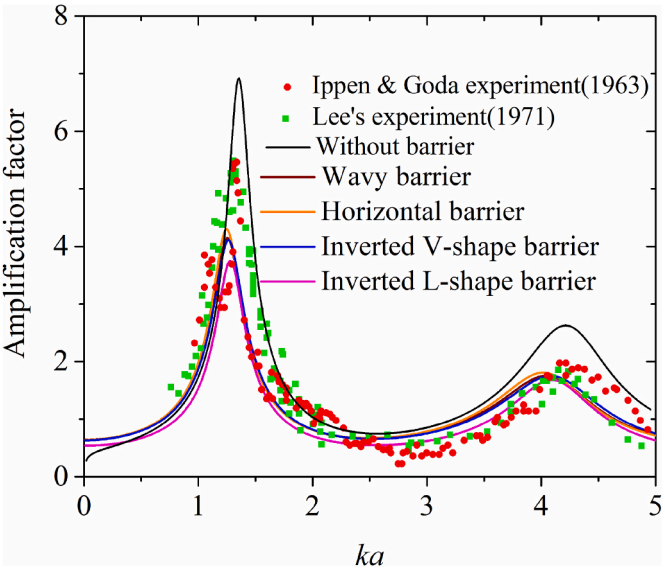

Fig. 4. The amplification factor of the present numerical scheme is compared with the experimental outcomes of Ippen and Goda (1963) and Lee (1971) at the back wall of the rectangular port.

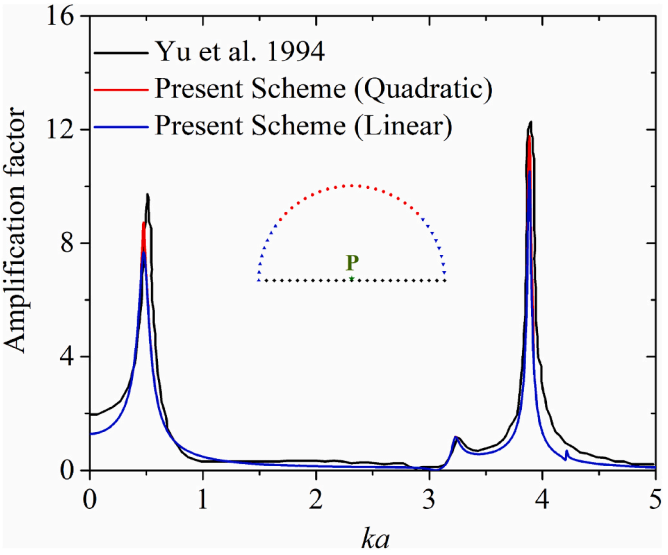

Fig. 5. Comparison of amplification factor of the present numerical scheme for the nonlinear (quadratic) pressure drop and linear pressure drop having a fully reflective port and normal incident wave with the analytical solution of Yu and Chwang (1994).

The boundary of the rectangular port, including the porous barriers, is discretized utilizing the spectral discretization, and the total number of grid points is 347 at the non-degenerate boundary, i.e., wall of the port and pseudo boundary, the port wall is denoted with blue grid points (Fig. 3) including pseudo boundary denoted with green dots while the number of elements at the horizontal barrier, wavy barrier, inverted V-shaped barriers, and inverted L-shaped barriers is 40, 50, 40 and 58 respectively represented with red grid points in Fig. 3.

The simulation results are obtained for the rectangular port in the absence of a porous barrier and compared with the available experimental data of (Ippen and Goda, 1963; Lee, 1971) in the wave amplification graph corresponding to non-dimensional wave number (ka) with $a = 1.44$. The two different resonance modes are obtained from the present studies (Fig. 4) in the absence of a porous barrier approximately similar to the previous studies. The porous barrier of different configurations is considered with porosity $\mu = 0.5$, discharge coefficient $\alpha = 0.7$, and thickness $\delta = 1$ cm to analyze the dissipation efficiency. The wave amplification inside the port with porous barrier at degenerate boundary is reduced as compared to without barriers. Actually, the

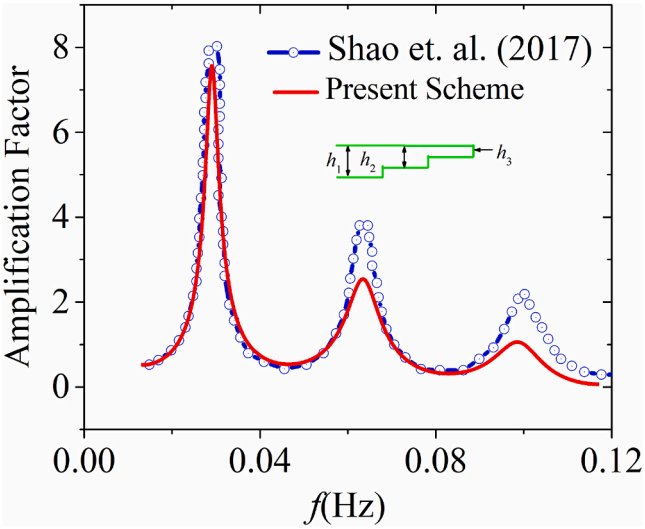

Fig. 6. Comparison of amplification factor of the present numerical scheme including variable depth inside the rectangular port with the analytical solution of Shao et al. (2017) is given for normal incident wave angle at the entrance.

primary function of the porous barrier reduces the wave energy transmission through it, which results in creating the calmer area. Thus, the current numerical model can be employed to include the influence of the porous barrier of any configuration at an arbitrary position inside the port.

Additionally, the validation of the current numerical model is conducted with the semi-circular port, including a pair of porous barriers at the pseudo boundary with linear and nonlinear pressure drop is carried out by comparing the amplification factor at the center of the back wall P (0,0) of the semi-circular harbor of radius $r = 0.5$ m with the analytical approximation of Yu and Chwang (1994). The comparisons of the current numerical scheme with the analytical approximation is presented in Fig. 5. In this analysis, a normal incident waves at the entrance with a complex porous effect $G = 0.001i$ for the linear pressure drop and the discharge coefficient $(\alpha = 0.4)$ for the nonlinear pressure drop are considered. On comparing, the linear pressure drop with the nonlinear pressure drop, there is a slight increase in the wave amplification factor as the nonlinear pressure drop includes the wave height effect in the energy dissipations.

Moreover, to demonstrate the validity of the present numerical scheme over varying bathymetric, the current numerical is compared with the previous analytical result of Shao et al., (2017). To include the variable bottom profile, the rectangular port of length 20 m and breadth 2 m is divided into three regions having depth $h_1 = 0.3$, $h_2 = 0.2$, and $h_3 = 0.1$ in the Region-II-A, Region-II-B, and Region-II-C, respectively. The amplification curve as a function of frequency response obtained at the back wall of the rectangular port is shown in Fig. 6 with variable depth. The three different resonant modes are estimated, which are approximately the same as in the previous study. There is a slight variation in resonant peak observed from the analytical study, as the slope ($s_1 = 0$ and $s_2 = 1/50$) are taken in the case of Shao et al. (2017) as compared to our scheme.

3.2. Convergence analysis

The convergence analysis determines the accuracy of the scheme and the pace at which errors tend to zero by increasing the number of boundary grid points and is described by the order of convergence. The least-square method (LSM) is used to obtain the order of convergence, and iterative approach are utilize to determine the error norm as grid discretization increases. The harbor's boundary is discretized into M_1, M_2, M_3, M_4, M_5 and M_6 number of grid points and the error norm is defined as follows:

$$E_{M_i} = \|\varphi_{M_i}(\vec{x}) - \varphi_{M_\infty}(\vec{x})\|_2 = \frac{c}{M_i^\theta} \tag{50}$$

where M_i represents the number of grid points for the ith iterations, and M_∞ represents the total number of grid points in maximum number of iterations to determine the order of convergence. In this study, the five iterations are considered, i.e. $M_\infty \approx M_6$, θ represents the order of convergence, and c is the constant to be determined by substituting $i = 1, 2, 3, 4, 5$ in Eq. (50).

The boundary of the rectangular port, including a degenerate horizontal porous barrier along the side of the entrance (Fig. 3a) is discretized by using regular discretization and spectral discretization into $M_1 = 60$, $M_2 = 120$, $M_3 = 240$, $M_4 = 480$, $M_5 = 960$ and $M_6 = 1920$ number of boundary grids. The convergence analysis for the rectangular port including horizontal porous barrier is shown in Fig. 7, and the convergence order for the spectral discretization and regular discretization is approximated as 1.74 and 1.5, respectively. The numerical

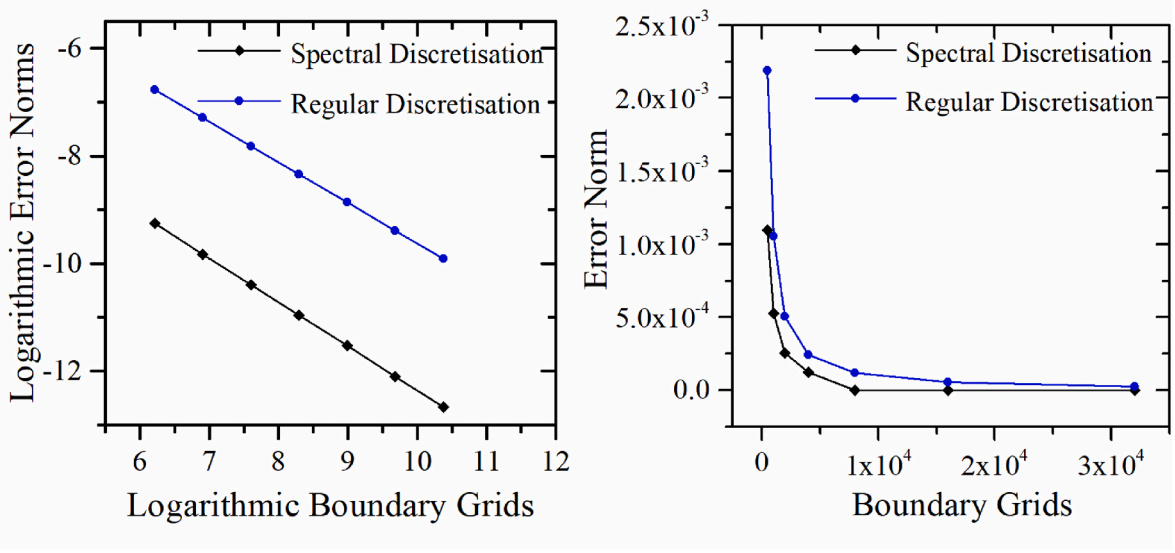

Fig. 7. The logarithmic error norm in (a) and the error norm in (b) with the convergence order is 1.509 and 1.7412 approximated by the use of LSM and iterative method for the Dual BEM with regular discretization and spectral discretization, respectively.

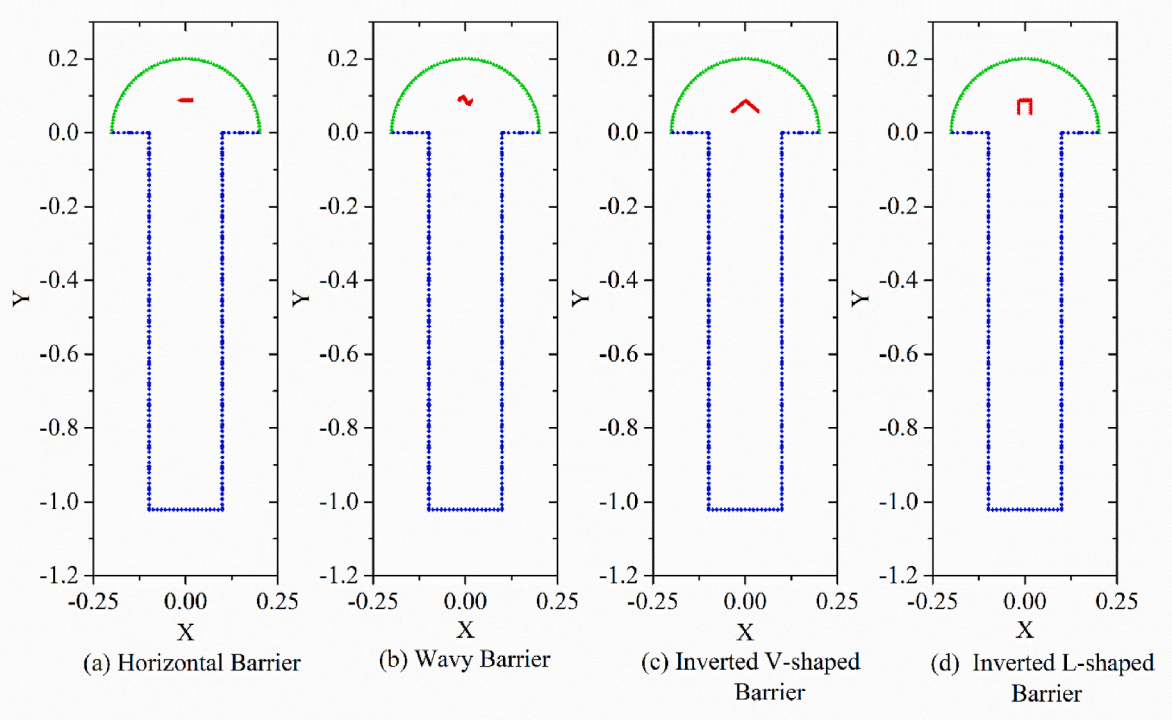

Fig. 8. The domain discretization of the rectangular port includes the degenerate barrier (a) Horizontal barrier, (b) Wavy barrier, (c) Inverted V-shaped barrier, and (d) Inverted L-shaped porous barriers at the center near the entrance.

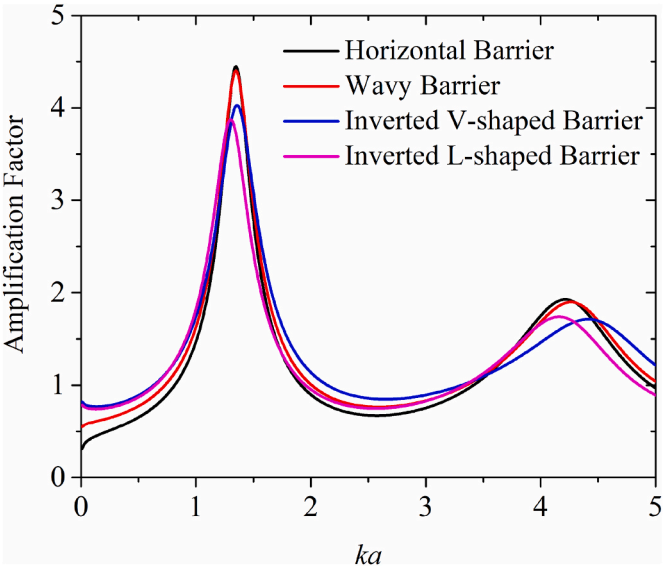

Fig. 9. The amplification factor of the present numerical scheme at the back wall of the rectangular port includes (a) Horizontal Barrier, (b) Wavy Barrier, (c) Inverted V-shaped barrier, and (d) Inverted L-shaped barrier at the center of the entrance.

scheme is stable as approximately converges to the real solution as the grid points increase. As given in Fig. 7, both regular and spectal discretization methods are consistence but the present numerical scheme with spectral point discretization provides higher convergence order.

4. Numerical simulations

4.1. Influence of porous barriers and partial reflection

The present numerical model is implemented on the simple shaped rectangular port including porous barriers and the singular and hyper singular integral equation is solved in the port region. The simulation result is obtained at the back wall of the rectangular port, including the influence of various configurations of the porous barrier. The spectral discretization is utilized to discretise the boundary of the confined domain is presented in Fig. 8. The boundary of the domain contains the non-degenerate boundary. Port's wall and pseudo boundary denoted with blue and green grid points, respectively, while the porous barrier/breakwaters of different configuration (horizontal, wavy, invert V-shape and L-shape) is treated as degenerate boundary placed at the center of the entrance, and it is denoted with red grid points. The boundary of the horizontal, wavy, inverted V-shaped, and inverted L-shaped porous barrier is discretized into 20, 25, 40, and 50 number grid points, respectively. The total 347 grid points are taken at the non-degenerate boundary of the rectangular port.

The amplification factoris plotted with respect to the non-dimensional wavenumber (ka) as the normal incident wave interacts with the rectangular port $R_{coeff} = 1$ having a length 1.208 m, width 0.198 m, and constant depth $h = 0.864$ (Fig. 9) at the back wall of the rectangular port. The porous barrier with different configurations as the horizontal, wavy, inverted V-shaped, and inverted L-shapedare constructed. In the present model, the influence of these porous barriers in terms of wave amplification is analyzed at the port's back wall with porosity $\mu = 0.5$, discharge coefficient $\alpha = 0.7$, and thickness $\delta = 1$ cm. It is observed that there are some variations in resonant peaks for the various configuration of porous barriers. The inverted L-shaped porous barrier contains a combination of vertical and horizontal barriers, illustrating a better hydrodynamic performance in mitigating the wave energy and thus reducing the wave amplification significantly as compared to all other porous barriers. Based on the simulation results, the inclusion of a porous barrier at right location proves an efficient tool in dissipating wave energy inside the port. The barrier configuration is also play an important role in analyzing the port'sresonance.

The numerical scheme is applied to the rectangular port to investigate the partially reflecting boundary of the port in the absence of porous barrier. The rectangular port is divided into two regions, Region-

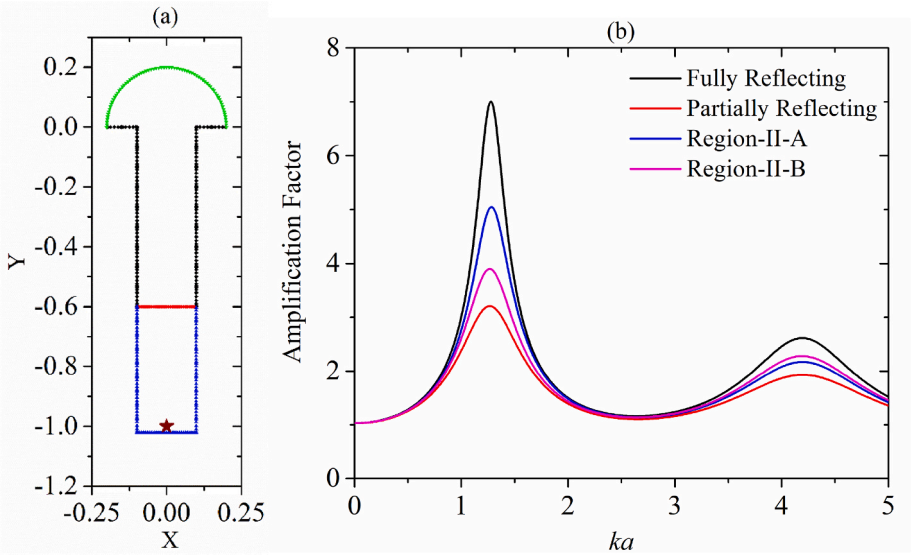

Fig. 10. The spectral discretization of the rectangular port Region-II-A and Region-II-B (a), and the amplification factor at the back wall of the rectangular port with fully and partially reflecting boundary of the port in the different basins.

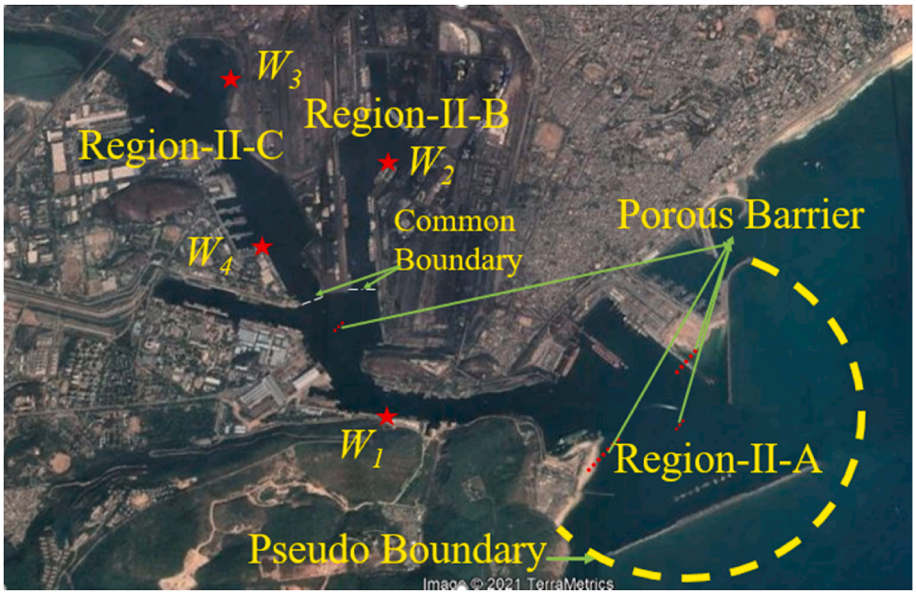

Fig. 11. Topographic image of Visakhapatnam port, Andhra Pradesh, India including pseudo-boundary denoted as yellow line and the common boundary interconnecting the Region-II-A with Region-II-B and Region-II-A with Region-II-C denoted with white dotted line. The four record stations from W_1 to W_4 marked with red star and the porous barrier denoted with red dotted line are considered at different locations.

II-A and Region-II-B, having constant depth denoted with black and blue dots connected with a common boundary, which is denoted with red grid points, and the pseudo boundary is denoted by green grid points (see Fig. 10a). The boundary of the confined domain is discretized utilizing the spectral discretization into 194, 164, 74, and 27 grid points, respectively, for the boundary of Region-II-A, Region-II-B, pseudo boundary, and common boundary. The simulation result is obtained at the back wall of the rectangular port marked with wine color stars in Fig. 10a and wave response graph is presented in Fig. 10b. In Fig. 10b, the black curve represents the fully reflecting ($R_{coeff} = 1$) boundary of the port whereas the red curve represents the partially reflecting ($R_{coeff} = 0.95$) boundary of each region of the port. The blue curve represents the partially reflecting ($R_{coeff} = 0.95$) boundary of Region-II-A and the fully reflecting ($R_{coeff} = 1$) boundary of Region-II-B, whereas pink curve represents the partially reflecting ($R_{coeff} = 0.95$) boundary of Region-II-B and the fully reflecting ($R_{coeff} = 1$) boundary of Region-II-A. It is observed from Fig. 10b, that the wave amplification for the various combinations of the boundary of the port reduces significantly with the consideration of the partially reflecting boundary of the port.

4.2. Visakhapatnam Port

Visakhapatnam Port, India, experiences 2.0–6.0 m during its extreme weather conditions and is situated on the East Coast in-between Kolkata in North and Chennai in South and its location in terms of latitude is 17.6856° N and longitude is 83.2160° E. The aerial view of Visakhapatnam Port is taken from Google earth pro and is shown in Fig. 11. Visakhapatnam Port is an ancient natural port that is covered with the Dolphin's Nose hill, and its prime location contributes significantly the trade and has trade relations with other countries and also with inter-

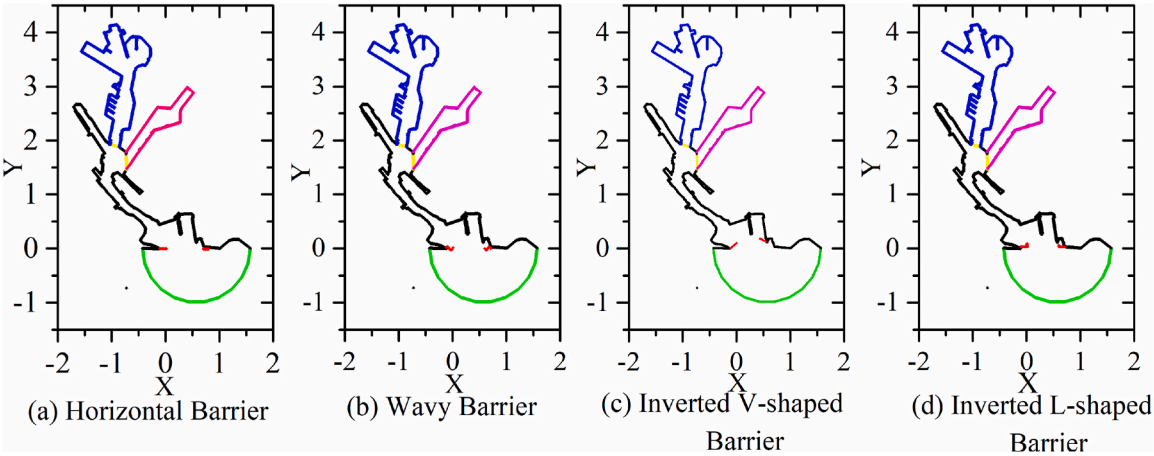

Fig. 12. The domain discretization of Visakhapatnam port, Andhra Pradesh, India, includes the degenerate barrier (a) Horizontal barrier, (b) Wavy barrier, (c) Inverted V-shaped barrier, and (d) Inverted L-shaped porous barriers at the two sides of the entrance.

state. Four record stations is marked with the red star (W_1 to W_4) to investigate the influence of porous barrier at the various location marked with red dotted line is shown in Fig. 11 and various configurations of porous barriers in the Visakhapatnam port are considered in the study. The annual cargo handling capacity is 125 million tons per annum, and the available facility to accommodate the ships of length up to 300 m, 36.0 m Beam, and 14.50 m draft in the Visakhapatnam port, Andhra Pradesh, India.

4.2.1. *Implementation on visakhapatnam port*

The current numerical scheme provides a platform to include the porous barrier of different shape at arbitrary positions with an ease to investigate the wave amplification in the presence of a porous barrier inside the multiconnected Visakhapatnam port. The numerical scheme is implemented on the actual topography of the Visakhapatnam port, India to analyze the resonance phenomenon. The Visakhapatnam port is divided into three interconnected regions, namely Region-II-A, Region-II-B, and Region-II-C. The actual bathymetry of the Visakhapatnam port lies in between 15 m and 28 m. The depth along the open sea domain is estimated at 28 m, and on moving towards the port, the depth of the bathymetry of the domain reduces. The approximate depth along the pseudo boundary, Region-II-A, Region-II-B and Region-II-C is estimated as 22 m, 18 m[1]6 m and 17 m, respectively. Thus the corresponding depth ratio is taken as $h_2/h_1 = 0.723$ and $h_3/h_1 = 0.773$, where h_1 represents the approximate depth for the Region-I, h_2 represents the depth for the Region-II-B, and h_3 is depth for the Region-II-C. The four distinct record stations W_1, W_2, W_3, and W_4 is marked in Fig. 11 inside the port to investigate the wave amplification in the presence of porous barrier/breakwaters. The thickness of the barrier is $\delta = 5$ cm, discharge coefficient $\alpha = 0.70$, and porosity is $\mu = 0.5$ is fixed.

4.2.2. *Influence of connected porous barriers*

The wave response inside the Visakhapatnam port in the presence of a pair porous barriers of different shapes is analyzed. The spectral point

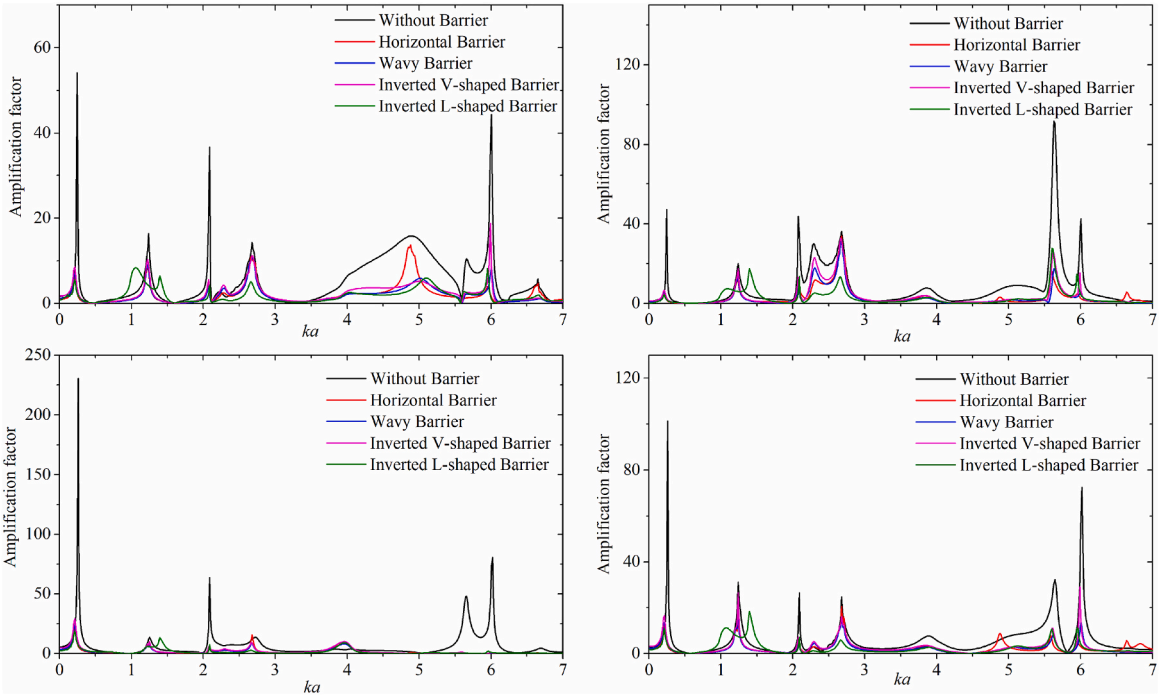

Fig. 13. The amplification factor at W_1 to W_4 inside the Visakhapatnam port with fully reflection ($R_{coeff} = 1$) including (a) Horizontal barrier, (b) Wavy barrier, (c) Inverted V-shaped barrier, and (d) Inverted L shaped porous barriers at the entrance is given for normal incident wave angle.

discretization is utilized to discretise the boundary of the port's interconnected regions, into $M_1 = 10780$, $M_2 = 3493$ and $M_3 = 8140$ number of grid points in Region-II-A, Region-II-B, and Region-II-C. The boundary of Region-II-A, Region-II-B, and Region-II-C is denoted with black, pink, and blue dots, respectively and pseudo boundary with green dots, discretise into $NP = 2501$ number of grid points. The common boundary connecting Region-II-A with Region-II-B and Region- II-A with Region-II-C is discretise into $p_1 = 250$, $p_2 = 150$, grid points denoted by yellow dots. The porous barrier is denoted with red dots and the boundary discretization of the horizontal barrier into $H_b = 100$ grid points, wavy barrier into $W_b = 150$ grid points, inverted V-shaped barrier into $V_b = 100$ grid points and inverted L - shaped barrier into $L_b = 180$ grid points.

The amplification at different record stations in the absence of a porous barrier and including porous barrier of various shapes is given in Fig. 13. Here, the normal incident wave is propagating at entrance at an angle 90° with the fully reflecting boundary of the port ($R_{coeff} = 1$). The six different resonance modes are obtained, i.e., $k_1 = 0.2448$, $k_2 = 1.2384$, $k_3 = 2.088$, $k_4 = 2.6784$, $k_5 = 5.6304$ and $k_6 = 6.0048$ for both the cases with and without porous barriers. The response curve reveals that the inclusion of porous barrier proves an efficient tool to reduce the wave amplification inside the realistic port. The amplification factor reduces significantly in the presence of porous barrier with different shapes. In addition, . The horizontal porous barrier and inverted V-shaped porous barriers shows higher amplification in comparison with other types of porous barriers while the inverted L-shaped porous barrier shows the least amplification. The surface area for the horizontal porous barrier and inverted V-shaped porous barriers are approximately same and having similiarinfluence over all the record stations (W_1 to W_4). The surface area of wavy barriers is greater than the horizontal and invertedV-shaped barriers and less than inverted L-shaped barrier.

The more surface area of the porous barrier allows maximal interaction with the incident waves and thus diminishes the wave oscillation inside the port.

4.2.3. *Influence of degenerate porous barriers*

The boundary discretization of the three interconnected regions and the porous barriers are placed at the center of the entrance is presented in Fig. (14). The total number of boundary grid points of each subregion, common boundary, and the pseudo boundary is the same as discussed in Fig. (12). The boundary of the horizontal barrier is discretized utilizing spectral point discretization into $H_b = 50$ grid points, wavy barrier into $W_b = 75$ grid points, inverted V-shaped barrier into $V_b = 50$ grid points and inverted L - shaped barrier $L_b = 90$ grid points. The porous barriers with different shapes are denoted with red grid points in Fig. 14.

The amplification factor is evaluated at locations W_1 to W_4 inside the Visakhapatnam port without and with porous barriers at the center of the entrance, as shown in Fig. 14. The incoming waves with normal incient wave angle at the entrance including the fully reflecting boundary of the port ($R_{coeff} = 1$) is considered. The wave amplification corresponding to the normalized wave frequency (ka) is estimated in Fig. 15. It is observed that the same resonance modes are obtained with as the porous barrier and without porous barriers. The wave amplification reduces effectively for the different shapes of porous barriers at the six resonance modes. It is seen from the wave amplification curve that variousshapes of porous barriers having different surface area placed at the center of the entrance does not show significant variations. Thus, the location of the porous barriers is also plays a significant role in developing the wave energy dissipator along the coastal region.

4.2.4. *Influence of degenerate porous barrier in the interior*

The computational domain is discretized into the finite number of boundary grid points utilizing spectral point discretization. The total number of boundary grid points at the pseudo boundary and the interconnected port regions, including its common boundary, is the same as in Fig. (12). In Fig. 16, the horizontal, wavy, inverted V-shaped, and inverted L-shaped porous barrier is discretized into 50, 75, 50, and 90 grid points, respectively. The porous barriers of different shapes are placed in the center of the interior of the port to analyze its significance on the wave oscillation.

The wave response ofdifferent types of porous barriers is investigated when the porous barrier is placed at the center of the interior of the Visakhapatnam port (see Fig. 17). The abscissa is taken as the normalized wave number, and the ordinate is the absolute value of the amplification factor. The wave amplification reduces significantly with the different shapes of porous barriers in the interior of the port, and the six t resonant peaks are obtained in the absence of the porous barriers. The amplification factor have strong resonace without porous barriers inside the four key locations of Visakhapatnam port. There is a significant reduction in wave amplification while utilizing the inverted L-shaped porous barriers as compared to other types of barriers. The main reason for reduction is that the surface area for the inverted L-shaped porous barriers are greater than the other porous barriers therefore, more wave dissipation are occurred in inverted L-shaped barrier.

4.2.5. *Influence of partial reflection*

Variations of the amplification factor curve for the Visakhapatnam port with the partially reflecting interconnected boundary of the port at all the four-record stations W_1 to W_4 is presented in Fig. 18. The black curve represents the fully reflecting ($R_{coeff} = 1$) boundary of the port, and the curve with the red line represents the partially reflecting ($R_{coeff} = 0.95$) boundary of the port. The response curve plotted in blue,

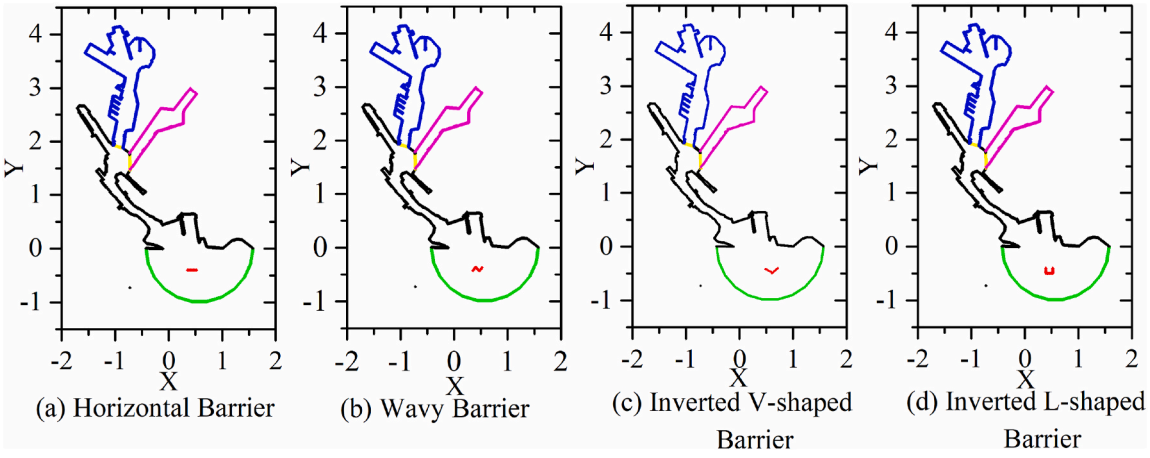

Fig. 14. The domain discretization of Visakhapatnam port, Andhra Pradesh, India, includes the four degenerate porous barriers (a) Horizontal barrier, (b) Wavy barrier, (c) Inverted V-shaped barrier, and (d) Inverted L-shaped porous barriers at the center of the entrance.

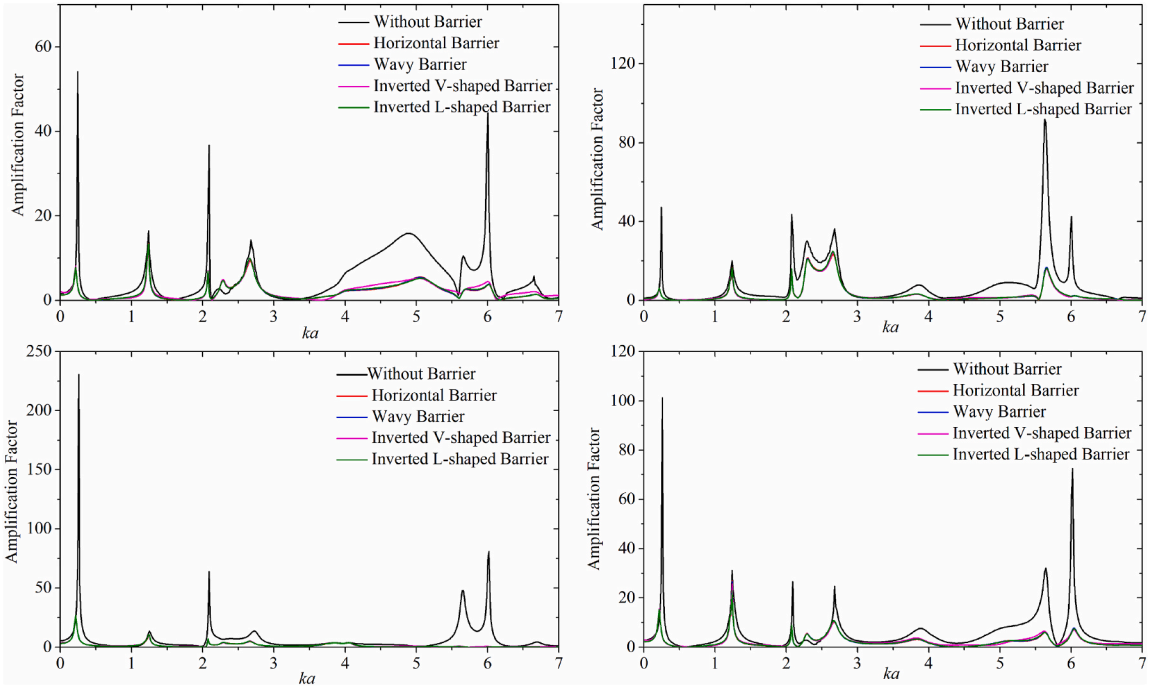

Fig. 15. The amplification factor at W_1 to W_4 inside the Visakhapatnam port with $R_{coeff} = 1$ including (a) Horizontal barrier, (b) Wavy barrier, (c) Inverted V-shaped barrier, and (d) Inverted L shaped porous barriers at the center of entrance is given for normal incident wave angle.

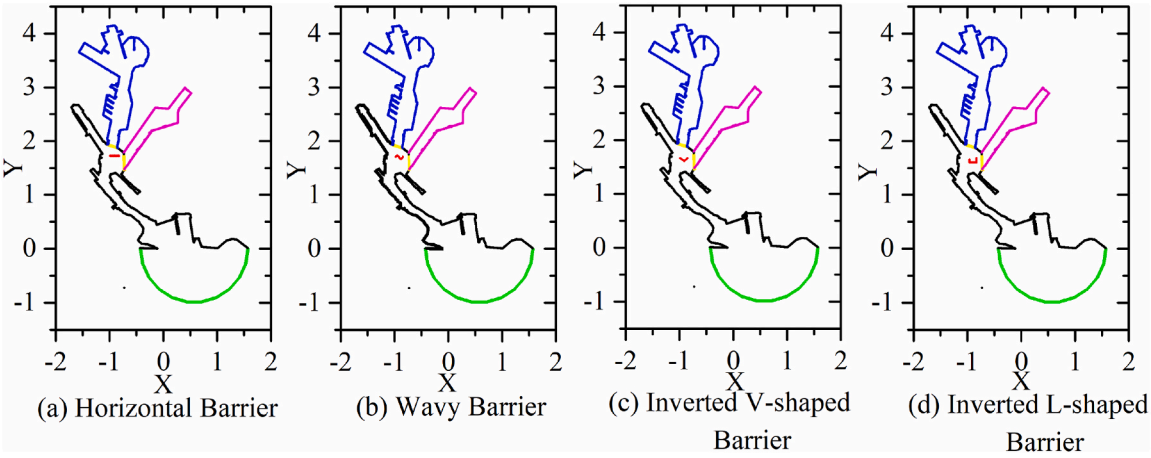

Fig. 16. The domain discretization of Visakhapatnam port, Andhra Pradesh, India, includes the degenerate barriers (a) Horizontal barrier, (b) Wavy barrier, (c) Inverted V-shaped barrier, and (d) Inverted L-shaped porous barriers at the interior of the port.

pink, and green lines denote the partially reflecting ($R_{coeff} = 0.95$) boundary of the Region-II-A, Region-II-B, and Region-II-C, respectively, while remaining boundary is treated as a fully reflecting ($R_{coeff} = 1$).

In real scenario, the boundary of the port can neither be fully reflective nor fully absorbing. Resonant peak reduces significantly for the partially reflecting boundary as compared with the fully reflecting boundary of the port. The behavior of the boundary of the port cannot be unanimous. Thus, simulation results are obtained to investigate the influence of partially reflecting boundaries of the different regions. The wave amplification of various combinations of partially reflecting boundaries of the port.

It is observed that the resonant peaks reduce effectively with the addition of partially reflecting boundaries of the port of Region-II-A, Region-II-B, and Region-II-C. Overall, it is found that the partially reflecting port boundaries and different subregions port boundaries can significantly reduce the wave oscillations as compared to the fully reflecting port boundaries.

4.2.6. *Influence of porous barrier*

In this study, the contour plot displays the distribution of wave height corresponding to resonant mode inside the Visakhapatnam port when a normal incident wave enters the port through a pseudo boundary and strikes the fully reflecting boundary of the port. In this analysis, Visakhapatnam port without porous barrier and porous barrier with porosity $\mu = 0.5$, discharge coefficient $\alpha = 0.7$ and thickness $\delta = 5$ cm is considered. The wave amplification contour plot for the first resonant mode ($k_1 = 0.2448$) without porous barrier and with the different types of porous barriers as horizotal, wavy, interveted V and interted L-shaped are placed at the entrance is presented in Fig. 19a. The wave amplitude contour for the sixth resonance mode ($k_6 = 6.008$) without porous barrier and with the different typesporous barriers as mentioned above are placed at the center of the interior of the port is given in Fig. 19b. The

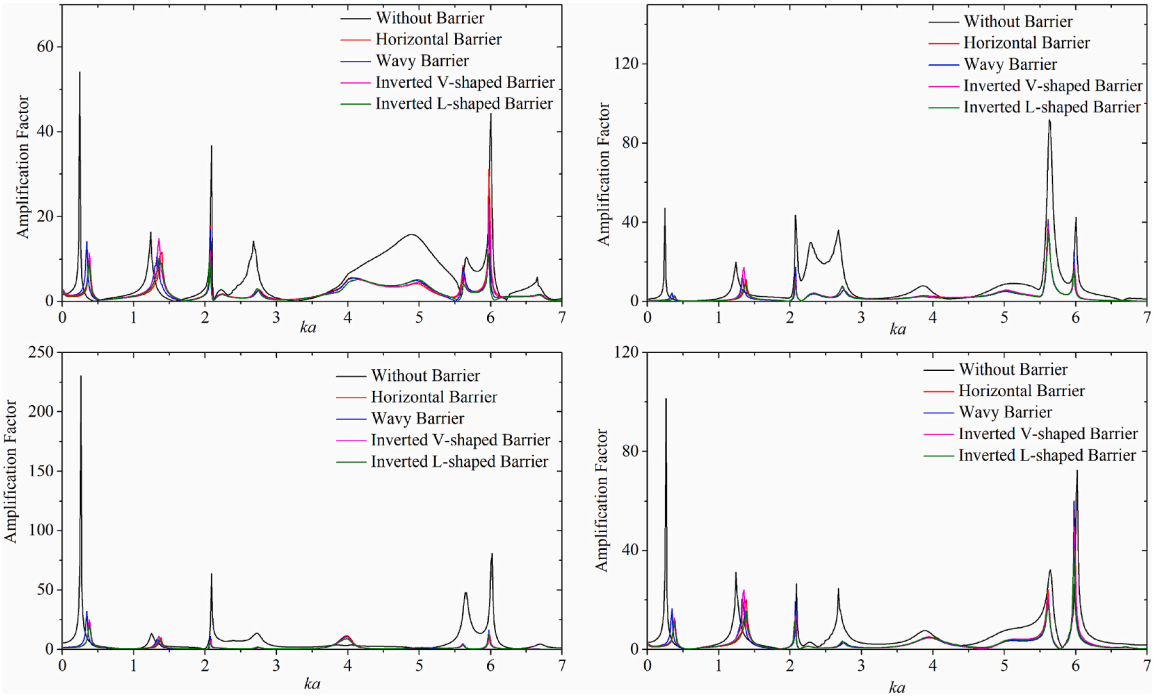

Fig. 17. The amplification factor at W_1 to W_4 inside the Visakhapatnam port with $R_{coeff} = 1$ including (a) Horizontal barrier, (b) Wavy barrier, (c) Inverted V-shaped barrier, and (d) Inverted L shaped porous barriers at the interior of the port is given for normal incident wave angle at the entrance.

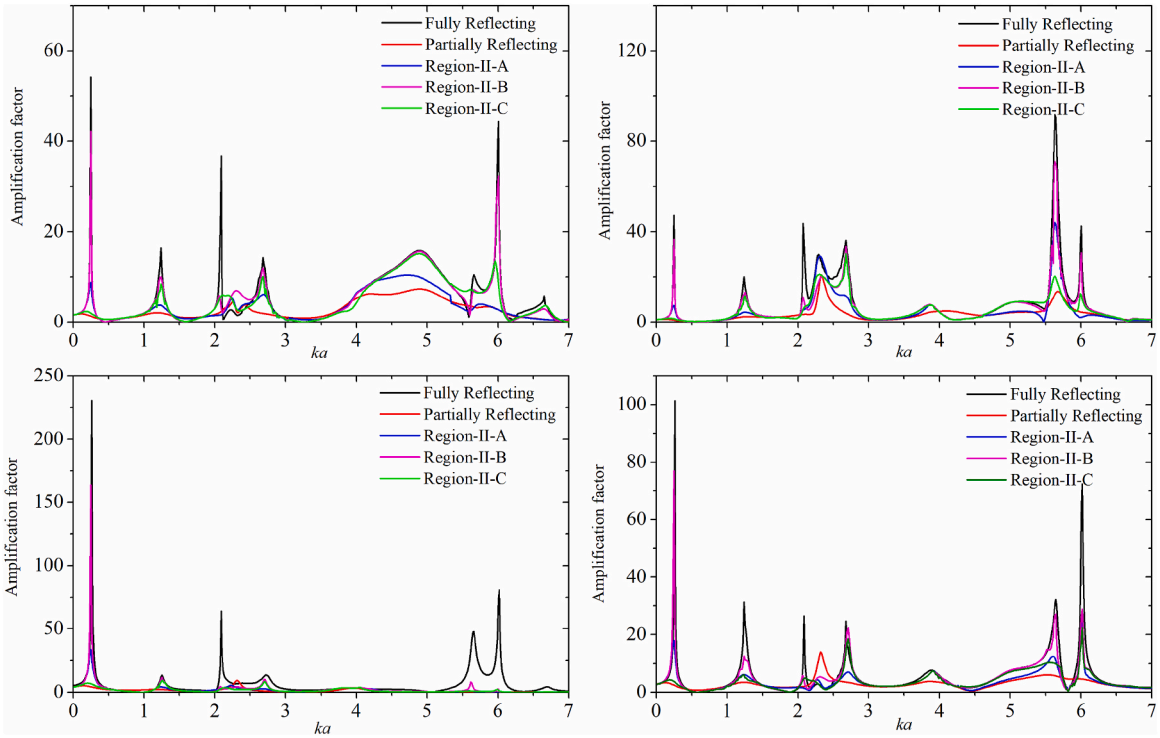

Fig. 18. The amplification factor at W_1 to W_4 inside the Visakhapatnam port with the partially reflecting port remaining other boundaries of the port are treated as the fully reflecting boundary ($R_{coeff} = 1$) is given for normal incident wave angle at the entrance.

effect of various porous barrier is investigated to demonstrate the improved hydrodynamic performance of the barriers inside the port.

The strong wave oscillation is observed in the Region-II-C near the third and fourth record stations, i.e., W_3 and W_4, in case of without porous barriers. The porous barrier at the two sides of the entrance reduces the wave amplification significantly in Region-II-C along with the W_3 and W_4. The influence of various types of porous barriers, the wave intensity for the inverted L-shaped porous barrier is less than the other barriers, while the horizontal and inverted V-shaped porous barrier shows similiarwave intensity but greater than the wave intensity for the wavy barrier.

The surface wave elevation for the sixth resonance mode is presented

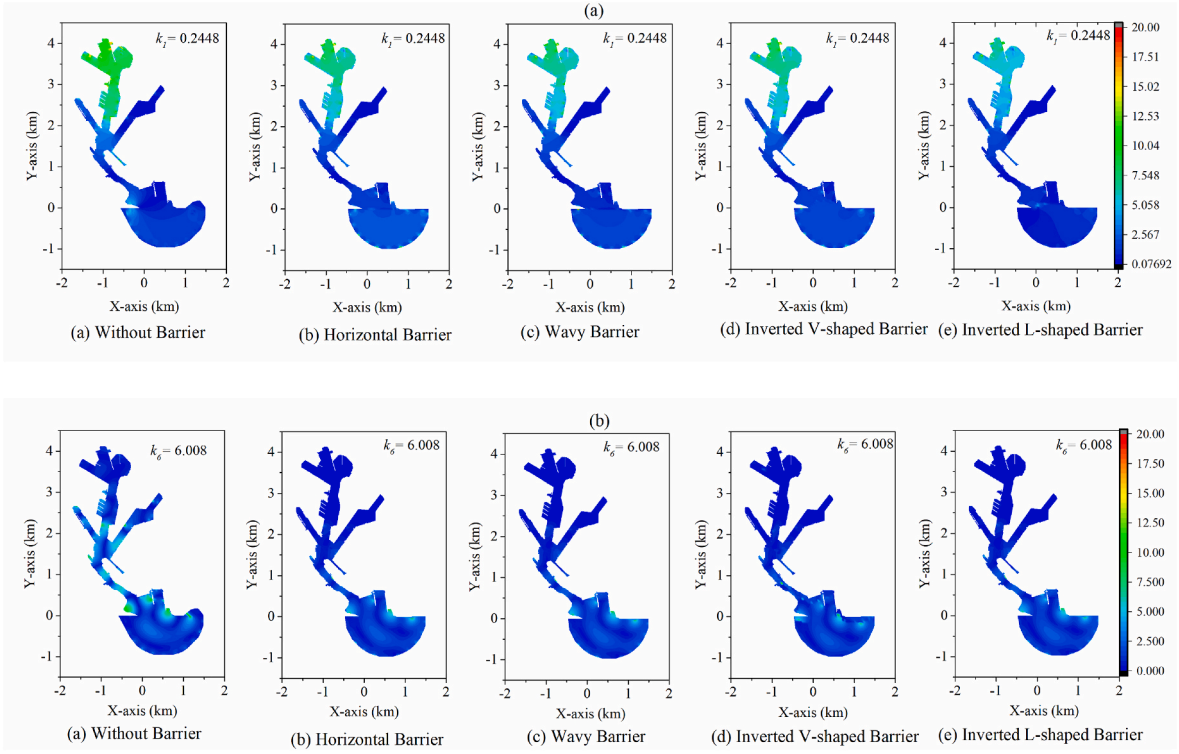

Fig. 19. Wave amplificationcontour without porous barrier and with the different types of porous barriers (horizontal, wavy, inverted V and inverted L) for the (a) first resonance mode k_1 and the connected porous barriers at the two sides of the entrance and (b) sixth resonance mode k_6 and the degenerate poruous barriers at the center of the interior of the port are given for normal incident wave angle at the entrance.

in Fig. 19b, the normal incident waves produced the high oscillation near the corner of the entrance. The contour plot with the inclusion of a porous barrier at the center of the interior of the port effectively reduces the wave elevation at the corner of the entrance including the entire port. The incident wave with normal incidence in the port produces high resonance while addition of porous barriers can significantly reduce the resonace in Visakhapatnam port. Therefore, adding a porous barrier/ breakwaters at different key location proves to be an efficient tool in protecting the coastal structures from the strong waves.

5. Conclusions

An efficient numerical scheme for the estimation of hydrodynamic performance by the porous barrier within the port is developed using DBEM in the arbitrarily shaped port. In addition, the variable bathymetry is also included in the present model with different shaped porous barriers. Firstly, the numerical model is utilized forvariety of porous barriers such as horizontal barrier, wavy barrier, inverted V-shaped barrier, and inverted L-shaped barrier having nonlinear pressure drop with partially reflecting boundary over the rectangular port.

The validity of the numerical scheme is obtained through the comparison of wave amplification factor for rectangular domain using DBEM, including the porous barriers as a degenerate boundary at the two sides of the entrance with the existing studies of experimental results. The numerical simulations is also compared with the analytical study of the semi-circular harbor with linear pressure drop and nonlinear pressure drop. The current numerical scheme is validated with the analytical study of Shao et al. (2017) of varying bathymetry. In addition, the convergence analysis forthe rectangular port with a horizontal barrier at the two sides of the entrance is conducted with spectral and regular discretization using least square and iterative method. The spectral discretization provides better accuracy as compare to the regular discretization.

The numerical scheme is applied to the rectangular port to study the influence of the porous barrier at the center of the entrance and connected porous barrier along the entrance. A significant reduction in wave amplification is observed for the different porous barriers. Further, numerical investigations are carried out to understand the effect of porous barriers in the Visakhapatnam port with different shapes. The wave amplification is estimated for the selected four key record stations (W_1 to W_4), and the six different resonance mode is obtained, i.e., $k_1 = 0.2448$, $k_2 = 1.2384$, $k_3 = 2.088$, $k_4 = 2.6784$, $k_5 = 5.6304$, and $k_6 = 6.0048$ in the port. The porous barrier of variousshapes as horizontal, wavy, inverted V and inverted L shapeshows the different effects on the wave amplification inside the port. In general, increase in surface area of porous barrier provides a maximal area for the wave dissipation, hencereduces the wave amplification. In this study, the porous barrier of inverted L-shaped allows the maximal surface area and thus reduces the wave oscillation significantly in comparison with other barriers. The study also concludes that porous barrier with different shapes as well as its location is also plays a significant role to analyze the resonance phenomenon. Moreover, the inclusion of various combinations of partially reflecting boundary of the port can effectively reduces the harbor resonance.

The ocean surface wave field is also determined in Visakhapatnam Port for the first and sixth resonant modes without barrier and with a different shapesof porous barriers are placed at the two sides of the entrance and at the interior of the port, respectively. The surface elevation in the interior of the port represents through the contour plot for the normal incident wave with a fully reflecting port wall. On the basis of the surface elevation contour plots, the area inside the port with strong and weak amplitude is identified, which aids in selecting the safest location for the loading and unloading of the moored ship and other water vessels under the resonance conditions. The resonance within the port can be considerably reduced by making appropriate changes to the Visakhapatnam port layout, such as erecting barriers of diverse configurations at different locations. As a result, energy dissipaters can be built as part of port alteration and planning to reduce

wave-induced oscillation to a certain amount. A current numerical approach is a useful tool for designing artificial port layouts, as well as for modifying existing harbor layouts to reduce resonance.

CRediT authorship contribution statement

Prachi Priya: Conceptualization, Methodology, Software, Data curation, Validation, Writing – original draft. **Prashant Kumar:** Conceptualization, Visualization, Writing – review & editing, Investigation, Supervision, Writing – review & editing. **Rajni:** Visualization, Investigation, Writing – review & editing.

Declaration of competing interest

The authors declare that they have no known competing financial interests or personal relationships that could have appeared to influence the work reported in this paper.

Data availability

Data will be made available on request.

Acknowledgment

This work was financially supported by the Department of Applied Science (Mathematics), National Institute of Technology, Delhi.

Annexure-I.

The four functions, $H_0^1(kr)$, $\frac{\partial H_0^1(kr)}{\partial n_s}$, $\frac{\partial H_0^1(kr)}{\partial n_f}$ and $\frac{\partial^2 (H_0^1(kr))}{\partial n_f \partial n_s}$ in the dual integral equations have different orders of singularity when kr approaches zero The key point of the problem is the utilization of the global and local coordinates transformation. The boundary element discretization of the arbitrary domain in global coordinates is shown in Fig. A1 (a), and the single element in the local coordinate is presented in Fig. A1 (b).

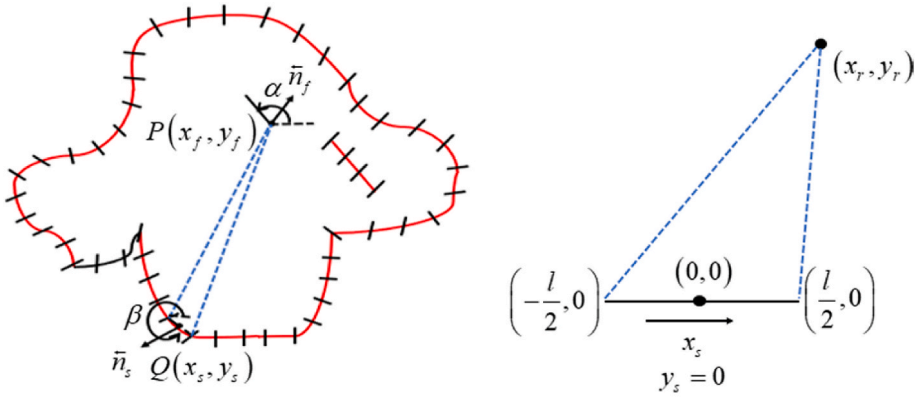

(a) **(b)**

Fig. A1. (a) The boundary discretization of arbitrary domain with the constant elements **(b)** coordinate transformation.

The relationship between global and local coordinates is illustrated in Fig. A1 (b), using the following transformation

$$\begin{aligned} x_r &= \cos\beta(x_f - x_s) + \sin\beta(y_f - y_s) \\ y_r &= -\sin\beta(x_f - x_s) + \cos\beta(y_f - y_s) \end{aligned} \tag{A1}$$

The components of the unit outer normal vectors are given as

$$n_{x_s} = \sin\beta, n_{y_s} = -\cos\beta, n_{x_f} = \sin\alpha, \text{and } n_{y_f} = -\cos\alpha \tag{A2}$$

(a) Integration of $H_0^1(kr)$ at singularity

The Hankel function $(H_0^1(kr))$ can be expressed in terms of Bessel functions by the equations:

$$H_0^1(kr) = J_0(kr) + iY_0(kr) \tag{A3}$$

The value of the Hankel function is known for the known value of kr, as kr approaches zero the behavior of the Bessel functions is given

$$J_0(kr) \approx 1 \text{ as } kr \to 0 \tag{A4}$$

$$Y_0(kr) \approx \frac{2}{\pi}\left(\log\frac{kr}{2} + \gamma\right) \text{ as } kr \to 0 \tag{A5}$$

where $\gamma = 0.577216$ …. and is termed as Euler's constant.

The Hankel function shows the logarithmic singularity and can be evaluated by performing the following integration

$$\int H_0^1(kr)d\Gamma = \lim_{(x_r,y_r)\to(0,0)}\left[\int_{-0.5l}^{0.5l}\left(1+\frac{2}{\pi}i\left(\log\frac{kr}{2}+\gamma\right)\right)d\Gamma\right] = l+\frac{2}{\pi}i\gamma l + \lim_{(x_r,y_r)\to(0,0)}\left[\frac{2}{\pi}i\int_{-0.5l}^{0.5l}\log\frac{kr}{2}d\Gamma\right] = l+l\frac{2}{\pi}i\left[\log\frac{kl}{4}-1+\gamma\right] \tag{A6}$$

(b) Integration of $\frac{\partial H_0^1(kr)}{\partial n_s}$ at singularity

The normal derivative of Hankel function is given as

$$\frac{\partial H_0^1(kr)}{\partial n_s} = -kH_1^1(kr)\frac{\partial r}{\partial n_s} \tag{A7}$$

Where the Hankel function of first kind of first order $(H_1^1(kr))$ is expressed in terms of Bessel functions by the equations:

$$H_1^1(kr) = J_1(kr) + iY_1(kr) \tag{A8}$$

As *kr* approaches zero, the behavior of the Hankel function is given as follows:

$$J_1(kr) \approx 0 \text{ as } r\to 0 \tag{A9}$$

$$Y_1(kr) \approx -\frac{2}{\pi}\left(\frac{1}{kr}\right) \text{ as } kr\to 0 \tag{A10}$$

$$\int \frac{\partial H_0^1(kr)}{\partial n_s}d\Gamma = \lim_{(x_r,y_r)\to(0,0)}\left[\frac{2}{\pi}i\int_{-0.5l}^{0.5l}\left(\frac{1}{r}\frac{\partial r}{\partial n_s}\right)d\Gamma\right] \tag{A11}$$

In local coordinate systemsss

$$\frac{\partial r}{\partial n_s} = \frac{\partial r}{\partial x_s}n_{x_s} + \frac{\partial r}{\partial y_s}n_{y_s} = \frac{y_r}{r} \tag{A12}$$

On substituting Eq. (A12) in Eq. (A11), the integral becomes

$$\int \frac{\partial H_0^1(kr)}{\partial n_s}d\Gamma = \lim_{(x_r,y_r)\to(0,0)}\left[\frac{2}{\pi}i\int_{-0.5l}^{0.5l}\left(\frac{1}{r}\frac{y_r}{r}\right)d\Gamma\right] = \lim_{(x_r,y_r)\to(0,0)}\left[\frac{2}{\pi}i\int_{-0.5l}^{0.5l}\left(\frac{y_r}{(x_r-x_s)^2+y_r^2}\right)dx_s\right] = \lim_{(x_r,y_r)\to(0,0)}\left[\frac{2}{\pi}i\left[\tan^{-1}\left(\frac{x_r-x_s}{y_r}\right)\right]_{x_s=-0.5}^{x_s=-0.5}\right] = 2i \tag{A13}$$

(c) Integration of $\frac{\partial H_0^1(kr)}{\partial n_f}$ at singularity

The normal derivative of Hankel function is given as

$$\frac{\partial H_0^1(kr)}{\partial n_f} = -kH_1^1(kr)\frac{\partial r}{\partial n_f} \tag{A14}$$

where $\frac{\partial r}{\partial n_f} = \frac{\partial r}{\partial x_r}\frac{\partial x_r}{\partial n} + \frac{\partial r}{\partial y_r}\frac{\partial y_r}{\partial n}$, $\frac{\partial x_r}{\partial n} = \sin(\alpha-\beta)$ and $\frac{\partial y_r}{\partial n} = -\cos(\alpha-\beta)$.

The Hankel function shows the singularity as *kr* approaches to zero and is evaluated by

$$\int \frac{\partial H_0^1(kr)}{\partial n_f}d\Gamma = -k\int_{-0.5l}^{0.5l}H_1^1(kr)\frac{\partial r}{\partial n_f}d\Gamma = \frac{2}{\pi}i\int_{-0.5l}^{0.5l}\frac{1}{r}\frac{\partial r}{\partial n_f}d\Gamma = \lim_{(x_r,y_r)\to(0,0)}\frac{2i}{\pi}\left[-\frac{\sin(\alpha-\beta)}{2}\log\left[(x_r-x_s)^2+y_r^2\right]-\cos(\alpha-\beta)\tan^{-1}\left(\frac{x_r-x_s}{y_r}\right)\right]_{x_s=-0.5l}^{x_s=0.5l} = -2i \tag{A15}$$

(d) Integration of $\frac{\partial^2 H_0^1(kr)}{\partial n_f \partial n_s}$ at singularity

The second order normal derivative of Hankel function is given as

$$\frac{\partial^2 H_0^1(kr)}{\partial n_f \partial n_s} = -k\frac{\partial}{\partial n_f}\left[H_1^1(kr)\frac{\partial r}{\partial n_s}\right] \tag{A16}$$

The integration of second order Hankel function and utilizing the behavior of Hankel function for the first order as *kr* approaches zero is given as

$$\int \frac{\partial^2 H_0^1(kr)}{\partial n_f \partial n_s}d\Gamma = -k\frac{2}{\pi}i\lim_{(x_r,y_r)\to(0,0)}\int_{-0.5l}^{0.5l}\frac{\partial}{\partial n_f}\left[\frac{1}{kr}\frac{\partial r}{\partial n_s}\right]d\Gamma = -\frac{2}{\pi}i\lim_{(x_r,y_r)\to(0,0)}\int_{-0.5l}^{0.5l}\frac{\partial}{\partial n_f}\left[\frac{1}{r}\frac{\partial r}{\partial n_s}\right]d\Gamma \tag{A17}$$

The solution is obtained by using integration by parts and using Eq. (A12), is given as

$$\int \frac{\partial^2 H_0^1(kr)}{\partial n_f \partial n_s} d\Gamma = -\frac{2}{\pi} i \lim_{(x_r,y_r)\to(0,0)} \int_{-0.5l}^{0.5l} \frac{\partial}{\partial n_f}\left[\frac{y_r}{r^2}\right] d\Gamma = \frac{2}{\pi} i \lim_{(x_r,y_r)\to(0,0)} \left[-y_r \sin(\alpha-\beta) \frac{1}{(x_r-x_f)^2+y_r^2} - \cos(\alpha-\beta) \frac{(x_r-x_f)}{(x_r-x_f)^2+y_r^2} \right]_{-0.5l}^{0.5l} = \frac{8}{l\pi} i \tag{A18}$$

References

An, S., Faltinsen, O.M., 2012. Linear free-surface effects on a horizontally submerged and perforated 2D thin plate in finite and infinite water depths. Appl. Ocean Res. 37, 220–234.

Bakhti, Y., Chioukh, N., Hamoudi, B., 2017. A multi-domain boundary element method to analyze the reflection and transmission of oblique waves from double porous thin walls. J. Mar. Sci. Appl. 16 (3), 276–285.

Bennett, G.S., McIver, P., Smallman, J.V., 1992. A mathematical model of a slotted wave screen breakwater. Coast. Eng. 18 (3–4), 231–249.

Chang, Y., Wang, E.H., 2017. A harbor resonance model with reflecting, absorbing and Transmitting boundaries. Open Construct. Build Technol. J. 11, 413–432.

Chen, K.H., Chen, J.T., Chou, C.R., Yueh, C.Y., 2002. Dual boundary element analysis of oblique incident wave passing a thin submerged breakwater. Eng. Anal. Bound. Elem. 26, 917–928.

Chen, K.H., Chen, J.T., Lin, S.Y., Lee, Y.T., 2004. Dual boundary element analysis of normal incident wave passing a thin submerged breakwater with rigid, absorbing, and permeable boundaries. J. Waterw. Port, Coast. Ocean Eng. 130 (4), 179–190.

Chen, J.T., Yueh, C.Y., Chang, Y.L., Wen, C.C., 2017. Why dual boundary element method is necessary? Eng. Anal. Bound. Elem. 76, 59–68.

Cho, I.H., Kim, M.H., 2013. Transmission of oblique incident waves by a submerged horizontal porous plate. Ocean. Eng. 61, 56–65.

Chou, C.R., Han, W.Y., 1993. Wave-induced oscillations in harbours with dissipating quays. Coastal Eng. Japan 36 (1), 1–23.

Chou, C.R., Han, W.Y., 1994. Oscillations induced by irregular waves in harbours. In: Proceedings of the 24th International Conference on Coastal Engineering ASCE, pp. 2987–3001. New York.

Dong, G., Wang, G., Ma, X., Ma, Y., 2010. Harbor resonance induced by subaerial landslide-generated impact waves. Ocean. Eng. 37, 927–934.

Dong, G., Gao, J., Ma, X., Wang, G., Ma, Y., 2013. Numerical study of low-frequency waves during harbor resonance. Ocean. Eng. 68, 38–46.

Dong, G., Zheng, Z., Gao, J., Ma, X., Dong, Y., Wu, H., 2020a. Experimental investigation on special modes with narrow amplification diagrams in harbor oscillations. Coast. Eng. 159, 103720.

Dong, G., Zheng, Z., Ma, X., Huang, X., 2020b. Characteristics of low-frequency oscillations in the Hambantota Port during the southwest monsoon. Ocean. Eng. 208, 107408.

Gaillard, P., 1982. Numerical calculation of seiche motions in harbours of arbitrary shape. In: Proceedings of the 18th International Conference on Coastal Engineering ASCE (Cape Town, South Africa).

Gao, J., Ma, Xiaozhou, Zang, J., Dong, G., Ma, Xiaojian, Zhu, Y., Zhou, L., 2020. Numerical investigation of harbor oscillations induced by focused transient wave groups. Coast. Eng. 158, 103670.

Gao, J., Ma, X., Dong, G., Zang, J., Zhou, X., Zhou, L., 2019a. Topographic influences on transient harbor oscillations excited by N-waves. Ocean. Eng. 192, 106548.

Gao, J., Ji, C., Gaidai, O., Liu, Y., Ma, X., 2017. Numerical investigation of transient harbor oscillations induced by N-waves. Coast. Eng. 125, 119–131.

Gao, J., Ma, X., Dong, G., Zang, J., Zhou, X., Zhou, L., 2019b. Topographic influences on transient harbor oscillations excited by N-waves. Ocean. Eng. 192.

Gao, J., Ma, X., Chen, H., Zang, J., Dong, G., 2021b. On hydrodynamic characteristics of transient harbor resonance excited by double solitary waves. Ocean. Eng. 219, 108345.

Gao, J., Ji, C., Gaidai, O., Liu, Y., 2016. Numerical study of infragravity waves amplification during harbor resonance. Ocean. Eng. 116, 90–100.

González-Marco, D., Sierra, J.P., Fernández de Ybarra, O., Sánchez-Arcilla, A., 2008. Implications of long waves in harbor management: the Gij'on port case study. Ocean Coast Manag. 51, 180–201.

Ham, S., Bathe, K.J., 2012. A finite element method enriched for wave propagation problems. Comput. Struct. 94, 1–12.

He, S.Y., Liu, Y., Zhao, Y., Li, H., 2021. New analytical solutions of oblique wave scattering by submerged horizontal perforated plates using quadratic pressure drop condition. Ocean. Eng. 220, 108444.

Hong, H.K., Chen, J.T., 1988. Derivations of integral equations of elasticity. J Eng Mech – ASCE 114 (6), 1028–1044.

Huang, Z., Li, Y., Liu, Y., 2011. Hydraulic performance and wave loadings of perforated/slotted coastal structures: a review. Ocean. Eng. 38 (10), 1031–1053.

Ippen, A.T., Goda, Y., 1963. Wave Induced Oscillations in Harbors: the Solution for a Rectangular Harbor Connected to the Open-Sea. Report No. 59. Hydrodynamics Laboratory, MIT.

Ijima, T., Chou, C.R., Yumura, Y., 1975. Wave scattering by permeable and impermeable breakwater of arbitrary shape. Coast. Eng. 1886–1905, 1974.

Isaacson, M., Qu, S., 1990. Waves in a harbour with partially reflecting boundaries. Coast. Eng. 14, 193–214.

Kaligatla, R.B., Koley, S., Sahoo, T., 2015. Trapping of surface gravity waves by a vertical flexible porous plate near a wall. Z. Angew. Math. Phys. 66 (5), 2677–2702.

Kirby, J.T., Wen, L., Shi, F., 2003. FUNWAVE 2.0 Fully Nonlinear Boussinesq Wave Model on Curvilinear Coordinates. Center for Applied Coastal Research Dept. of Civil & Environmental Engineering, University of Delaware, Newark.

Koley, S., Kaligatla, R.B., Sahoo, T., 2015. Oblique wave scattering by a vertical flexible porous plate. Stud. Appl. Math. 135 (1), 1–34.

Koley, S., Panduranga, K., Almashan, N., Neelamanic, S., Al-Ragumc, A., 2020. Numerical and experimental modeling of water wave interaction with rubble mound offshore porous breakwaters. Ocean. Eng. 218, 108218.

Kumar, P., Zhang, H., Yuen, D.A., Kim, K.I., 2013. Wave field analysis in a harbor with irregular geometry through boundary integral of Helmholtz equation with contributions. Comput. Fluids 88, 287–297.

Kumar, P., Gulshan, 2017. Extreme wave-induced oscillation in paradip port under the resonance conditions. Pure Appl. Geophys. 174 (12), 4501–4516.

Kumar, P., Priya, P., Rajni, 2021. Boundary element modeling of multiconnected ocean basin in Visakhapatnam port under the resonance conditions. China Ocean Eng. 35 (2), 662–675.

Kumar, P., Rupali, 2018. Modeling of shallow water waves with variable bathymetry in an irregular domain by using hybrid finite element method. Ocean. Eng. 165, 386–398.

Kumar, P., Priya, P., Rajni, 2022. Mathematical modelling of Visakhapatnam Port utilizing the porous and non-porous breakwaters with fnite depth green function. Ocean Dynam. 72 (7), 557–576.

Kumar, P., Gulshan, 2018. Theoretical analysis of extreme wave oscillation in Paradip Port using a 3-D boundary element method. Ocean. Eng. 164, 13–22.

Lee, J.J., 1971. Wave-induced oscillations in harbours of arbitrary geometry. J. Fluid Mech. 45 (2), 375–394.

Lee, H.S., Williams, A.N., 2002. Boundary element modeling of multidirectional random waves in a harbor with partially reflecting boundaries. Ocean. Eng. 29 (1), 39–58.

Liu, Philip L.F., Yoon, S.B., Dalrymple, R.A., 1986. Wave reflection from energy dissipation region. J. Waterw. Port, Coast. Ocean Eng. 112, 632–644.

Liu, Y., Li, Y.C., Teng, B., Dong, S., 2008. Wave motion over a submerged breakwater with an upper horizontal porous plate and a lower horizontal solid plate. Ocean. Eng. 35 (16), 1588–1596.

Liu, Y., Li, H.J., 2017. Iterative multi-domain BEM solution for water wave reflection by perforated caisson breakwaters. Eng. Anal. Bound. Elem. 77, 70–80.

Mattioli, F., 1981. Wave diffraction of breakwaters in the presence of a coastline. Appl. Ocean Res. 3, 37–42.

Ma, X., Zheng, Z., Gao, J., Wu, H., Dong, Y., Dong, G., 2021. Experimental investigation of transient harbor resonance induced by solitary waves. Ocean. Eng. 230, 109044.

Mercadé Ruiz, P., Ferri, F., Kofoed, J.P., 2017. Water-wave diffraction and radiation by multiple three-dimensional bodies over a mild-slope bottom. Ocean. Eng. 143, 163–176.

Molin, B., 2011. Hydrodynamic modeling of perforated structures. Appl. Ocean Res. 33 (1), 1–11. https://doi.org/10.1016/j.apor.2010.11.003.

Molin, B., Remy, F., 2015. Inertia effects in TLD sloshing with perforated screens. J. Fluid Struct. 59, 165–177. https://doi.org/10.1016/j.jfluidstructs.2015.09.004.

Nishad, C.S., Vijay, K.G., Neelamani, S., Chen, J.T., 2021a. Dual BEM for wave scattering by an H-type porous barrier with nonlinear pressure drop. Eng. Anal. Bound. Elem. 131, 280–294.

Nishad, C.S., Vijay, K.G., Neelamani, S., Sekhar, G.P.R., 2021b. Dual Boundary Element Analysis for a Pair of Inverted T-type Porous Barriers Having Nonlinear Pressure Drop. Waves Random Complex Media, pp. 1–25. https://doi.org/10.1080/17455030.2021.1948145.

Panchang, V., Zhang, J., Demirbilek, Z., 2008. Incorporating rubble mound jetties in elliptic harbor wave models. J. Waterw. Port, Coast. Ocean Eng. 134, 40–52.

Rageh, O.S., Koraim, A.S., 2010. Hydraulic performance of vertical walls with horizontal slots used as breakwater. Coast. Eng. 57, 745–756.

Rupali, Kumar, P., 2021. Mathematical modeling of arbitrary shaped harbor with permeable and impermeable breakwaters using hybrid finite element method. Ocean. Eng. 221, 108551.

Shao, D., Feng, X., Feng, W.B., Hong, G.W., 2017. Harbor oscillations on a piecewise bottom of two different slopes. J. Mar. Sci. Technol. 22, 633–654.

Suh, K.D., Ji, C.H., Kim, B.H., 2011. Closed-form solutions for wave reflection and transmission by a vertical slotted barrier. Coast. Eng. 58 (12), 1089–1096.

Sulisz, W., 2015. Wave propagation in a converging channel of arbitrary configuration. China Ocean Eng. 29, 771–782.

Sulisz, W., 2005. Wave propagation in channel with side porous caves. J. Waterw. Port, Coast. Ocean Eng. 131, 162–170.

Venkateswarlu, V., Vijay, K.G., Nishad, C.S., 2021. Iterative dual boundary element analysis of a wavy porous plate near an inclined seawall. Ocean. Eng. 235 (2021), 109242.

Vijay, K.G., Venkateswarlu, V., Nishad, C.S., 2021. Wave scattering by inverted trapezoidal porous boxes using dual boundary element method. Ocean. Eng. 219, 108149.

Yip, T.L., Sahoo, T., Chwang, A.T., 2001. Wave oscillation in a circular harbor with porous wall. J. Appl. Mech. 68 (4) https://doi.org/10.1115/1.1379955.

Yu, X., Chwang, A.T., 1994. Wave-induced oscillation in harbor with Porous breakwaters. J. Waterw. Port, Coast. Ocean Eng. 120, 125–144. https://doi.org/10.1061/(ASCE)0733-950X(1994)120:2(125).

Zhao, Y., Liu, Y., Li, H., 2018. Iterative analytical solution for wave scattering by multiple partially immersed slotted barriers. In: The 28th International Ocean and Polar Engineering Conference. International Society of Offshore and Polar Engineers.

Zhao, Y., Liu, Y., Li, H., 2020a. Iterative analytical solution for wave reflection by a multi-chamber partially perforated caisson breakwater. Acta Oceanol. Sin. 39 (7), 115–126. https://doi.org/10.1007/s13131-020-1622-0, 2020.

Zhao, Y., Liu, Y., Li, H.J., Chang, A.T., 2020b. Iterative dual BEM solution for water wave scattering by breakwaters having perforated thin plates. Eng. Anal. Bound. Elem. 120, 95–106.

Zheng, Z., Ma, X., Ma, Y., Perlin, M., Dong, G., 2021. Numerical investigation of seismic induced harbor oscillations. Coast. Eng. 165, 103838.